

A Random Matrix Approach for Quantifying Model-Form Uncertainties in Turbulence Modeling

Heng Xiao^{a,*}, Jian-Xun Wang^a, Roger G. Ghanem^b

^a*Department of Aerospace and Ocean Engineering, Virginia Tech, Blacksburg, VA 24060, United States*

^b*Department of Aerospace and Mechanical Engineering, University of Southern California, Los Angeles, CA 90089, United States*

Abstract

With the ever-increasing use of Reynolds-Averaged Navier–Stokes (RANS) simulations in mission-critical applications, the quantification of model-form uncertainty in RANS models has attracted attention in the turbulence modeling community. Recently, a physics-based, nonparametric approach for quantifying model-form uncertainty in RANS simulations has been proposed, where Reynolds stresses are projected to physically meaningful dimensions and perturbations are introduced only in the physically realizable limits (Xiao et al., 2015. Quantifying and reducing model-form uncertainties in Reynolds-averaged Navier–Stokes simulations: An open-box, physics-based, Bayesian approach, arXiv:1508.06315). However, a challenge associated with this approach is to assess the amount of information introduced in the prior distribution and to avoid imposing unwarranted constraints. In this work we propose a random matrix approach for quantifying model-form uncertainties in RANS simulations with the realizability of the Reynolds stress guaranteed, which is achieved by construction from the Cholesky factorization of the normalized Reynolds stress tensor. Furthermore, the maximum entropy principle is used to identify the probability distribution that satisfies the constraints from available information but without introducing artificial constraints. We demonstrate that the proposed approach is able to ensure the realizability of the Reynolds stress, albeit in a different manner from the physics-based approach. Monte Carlo sampling of the obtained probability distribution is achieved by using polynomial chaos expansion to map independent Gaussian random fields to the Reynolds stress random field with the marginal distributions and correlation structures as specified. Numerical simulations on a typical flow with separation have shown physically reasonable results, which

*Corresponding author. Tel: +1 540 231 0926
Email address: hengxiao@vt.edu (Heng Xiao)

verifies the proposed approach. Therefore, the proposed method is a promising alternative to the physics-based approach for model-form uncertainty quantification of RANS simulations. The method explored in this work is general and can be extended to other complex physical systems in applied mechanics and engineering.

Keywords: model-form uncertainty quantification, turbulence modeling, Reynolds-Averaged Navier–Stokes equations, random matrix theory, maximum entropy principle

Notations

We summarize the convention of notations below because of the large number of symbols used in this paper. The general conventions are as follows:

1. Upper case letters with brackets (e.g., $[R]$) indicate matrices or tensors; lower case letters with arrows (e.g., \vec{v}) indicate vectors; undecorated letters in either upper or lower cases indicate scalars. An exception is the spatial coordinate, which is denoted as x for simplicity but is in fact a 3×1 vector. Tensors (matrices) and vectors are also indicated with index notations, e.g., R_{ij} and v_i with $i, j = 1, 2, 3$. In this paper, i and j are used with tensor indices while α and β are used as general indexes, e.g., for the modes of Kahunen–Loeve expansion or for the terms in the polynomial chaos expansion.
2. Bold letters (e.g., $[\mathbf{R}]$) indicate random variables (including scalars, vectors, and matrices), the non-bold letters (e.g., $[R]$) indicate the corresponding realizations, and underlined letters (e.g., $[\underline{R}]$) indicate the mean.
3. Symbols \mathbb{M}_d^s , M_d^+ , and \mathbb{M}_d^{+0} indicate the sets of symmetric, symmetric positive definite, and symmetric positive semi-definite matrices, respectively, of dimension $d \times d$ with the following relation: $\mathbb{M}_d^s \subset M_d^+ \subset \mathbb{M}_d^{+0}$.

This work deals with Reynolds stresses, which are rank two tensors. Therefore, it is implied throughout the paper that all random or deterministic matrices have sizes 3×3 with real entries unless noted otherwise. Finally, a list of nomenclature is presented in [Appendix B](#).

1. Introduction

Numerical models based on Reynolds-Averaged Navier–Stokes (RANS) equations are the dominant tool for the prediction of turbulent flows in industrial and natural processes.

For many flows the predictions from RANS simulations have large uncertainties, which are mostly attributed to the phenomenological closure models for the Reynolds stresses [1, 2]. Previous efforts in quantifying and reducing model uncertainties in RANS simulation have mostly followed parametric approaches, e.g., by perturbing, tuning, or inferring the model parameters in these closure models [3]. Recently, researchers in the turbulence modeling community have recognized the limitations of the parametric approach and started exploring nonparametric approaches where uncertainties are directly injected into the Reynolds stresses [2, 4–7].

In their pioneering work, Iaccarino and co-workers [4, 5] projected the Reynolds stress onto the six physically meaningful dimensions (its magnitude, shape, and orientation) and perturbed the Reynolds stresses towards the limiting states in the physically realizable range. Xiao et al. [7] utilized the six physical dimensions as the basis to parameterize the Reynolds stress uncertainty space, and the physical-based parameterization is further used for systematic exploration of the space and for Bayesian inferences to incorporate observation data. However, although the physics-based parameterization allows for a full representation of the uncertainty space, two limitations need to be addressed. First, the realizability constraints on Reynolds stresses provide guidance only on the shape of the Reynolds stress (in the form of the classical Lumley triangle [8] or the recently proposed Barycentric triangle [9]). In comparison, much weaker constraints can be imposed on the magnitude and the orientation, except for the constraint that the magnitude (i.e., turbulent kinetic energy) must be positive. For this reason and partly due to stability considerations, previous works on injecting uncertainty to the physical projections of the Reynolds stress have focused on the shape and magnitude [4, 6, 7], and they did not introduce uncertainties to the orientations. Second, in the context of Bayesian inference of Reynolds stress uncertainties as pursued by Xiao and co-workers [7, 10, 11], it is not straightforward to specify a prior distribution on the physical variables. Xiao et al. [7] specified Gaussian priors for the Reynolds stress discrepancy in terms of the tensor shape parameters and the logarithmic of the magnitude. In principle the same prior can be specified for the orientation angles. However, it is not clear how much information is introduced into the prior with this choice of probability distributions (i.e., log-normal distribution for the magnitude and standard normal for others). Moreover, in lack of physical insight, it is not clear how large the variance for each physical variable should be compared to each other. Although the prior plays a minor role in the Ensemble Kalman filtering based inference with a moderate amount of data as studied in Xiao et al. [7], it can be of critical importance for pure uncertainty propagation as pursued by Iaccarino and

co-workers [4–6] and for Bayesian inferences with small amounts of data. In particular, it is critical that no artificial constraints are introduced with overly confident prior distributions.

The entropy measure of information has been proposed more than half a century ago [12]. Since then, the maximum entropy principle has been extensively used as the guideline to specify prior probability distributions for Bayesian inferences [13]. The principle states that out of all possible distributions that satisfy the constraints from available information, the probability distribution that has the maximum entropy is a good prior distribution. Since entropy is a measure of randomness, the maximum entropy distribution is the most non-committal and most random in the dimensions in which no information is available. Consequently, it introduces the least amount of information in addition to the specified constraints. While the maximum entropy principle has been used extensively in many disciplines such as communications [14] and image processing [15], the use of maximum entropy principle in conjunction with random matrix theory for quantifying model-form uncertainties in physical systems is only a recent development. Soize [16] was the first to derive the maximum entropy probability distribution of a symmetric positive definite random matrices with a specified mean field. Applications to structural vibration problems were demonstrated, where the mass, stiffness, and damping matrices of the real system are described as random matrices with the corresponding matrices in the reduced model as their means. The framework was further extended to nonlinear structural dynamics problems and to other applications (e.g., composite materials [17], porous media[18]) and to problems with more complicated constraints, (e.g., on the variance of eigenvalues [18, 19], as well lower and upper bounds on the matrices [17]). See [20, 21] for comprehensive reviews of the recent development.

Since Reynolds stresses are symmetric positive definite tensors, it seems natural to use random matrix approach to describe the Reynolds stresses for the quantification of RANS modeling uncertainties. However, the authors' are not aware of any existing work in the literature that applied the random matrix theory in quantifying model-form uncertainties in RANS simulations. While many of the theories developed by Soize and co-workers can be applied here straightforwardly, an important characteristics of the RANS modeling application is that the Reynolds stresses are described by a random matrix field with spatial correlations. In contrast, the matrices in the previously investigated applications either involve only a few individual matrices (e.g., the mass, stiffness, and damping matrices in structural dynamics applications [16]) or a large number of random matrices without spatial correlation structure (e.g., the effective constitutive matrices in the meso-scale modeling of composite materials [17]). A notable exception is the recent work of Guillemintot [18], where

the permeability tensor is modeled as a random matrix field with a specified correlation structure.

In the present contribution, we use an approach based on the random matrix theory and the maximum entropy principle to quantify model-form uncertainties in RANS modeling. The objectives of this work are two-fold. First, the proposed framework for quantifying model form uncertainties in RANS simulations provides an alternative to the physics-based approach investigated by Iaccarino and co-workers [4–6] and Xiao and co-workers [7, 10, 11]. The advantages and disadvantages of both approaches can thus be contrasted and compared later on. Despite the better mathematical rigorousness of the maximum entropy approach, it is possible that the physics-based approach may still be preferred by RANS simulations practitioners for both uncertainty quantification and Bayesian inferences. This is because of its convenience in incorporating physical prior knowledge. As such, another objective and motivation for this work is to provide basis for gauging the departure of the priors used in the physics-based approach from the maximum entropy condition. By comparing the prior distributions of the obtained Reynolds stress from both approaches, the current framework can reveal the amount of information introduced in the physics-based prior distribution, and thus provide guidance for the choice of priors in the physics-based approach.

The rest of the paper is organized as follows. Section 2 introduces the realizability of Reynolds stresses in details and argues that the current framework of modeling Reynolds stress as positive semidefinite tensors can guarantee realizability in the same way as in the previously proposed physics-based approaches [7]. Section 3 introduces the random matrix framework for model-form uncertainty in RANS simulation and discusses its implementations. Section 4 uses the flow over periodic hills as an example application to demonstrate the performance of the proposed method. The probability measure of the obtained distribution on the limiting states is discussed in Section 5. Finally, Section 6 concludes the paper.

2. Realizability of Reynolds Stresses: Physical vs. Mathematical Perspectives

2.1. The Origin and History of Realizability Constraints

For incompressible flows, the RANS equations are obtained by decomposing the instantaneous velocity \mathbf{v}_i , into the mean quantity \underline{v}_i and its fluctuation \mathbf{v}'_i . That is, $\mathbf{v}_i = \underline{v}_i + \mathbf{v}'_i$. Note the bold letters used to denote the instantaneous velocity, indicating that it is considered a random variable. Substituting the decomposition above into the Navier Stokes equation leads to a covariance term $\langle \mathbf{v}'_i \mathbf{v}'_j \rangle$ of the velocity fluctuations. This term is referred

to as Reynolds stress and is denoted as R_{ij} for simplicity¹, but the covariance nature of this term has profound implications. Specifically, a Reynolds stress tensor must be symmetric positive semi-definite, i.e., $R_{ij} \in \mathbb{M}_3^{+0}$, where \mathbb{M}_3^{+0} is the set of symmetric positive semidefinite matrices. In fact, the Reynolds stresses are mostly positive definite (i.e., all eigenvalues are positive), i.e., $R_{ij} \in \mathbb{M}_3^+$, and zero eigenvalues occur only in extreme cases, e.g., on the wall boundaries or in turbulence-free regions, where velocity fluctuations for one or more components are zero. For practical purposes it is not essential to distinguish between \mathbb{M}_3^+ and \mathbb{M}_3^{+0} when quantifying model form uncertainties in RANS simulations.

For a tensor to be a valid Reynolds stress tensor, or equivalently, to be physically realizable, there must exist a velocity that has this covariance. The physical realizability of Reynolds stresses and the associated second-order closure models were a topic of intensive research in the early years of turbulence model development. Early works of Schumann [23], Lumley [24], and Pope [25], among others, have lead to a class of realizable second-order closure models [26]. Since these models solve an evolution equation for the Reynolds stresses, these models guarantee the realizability by imposing certain constraints on the rate of change $[\dot{R}]$ of the Reynolds stress, i.e., the constraint that its principle stress components (e.g., eigenvalues) do not further decrease when at zero [25]. The well known Lumley triangle [8] provided a map for all realizable turbulence by projecting the Reynolds stress to a plane. Specifically, the following decomposition is performed on the Reynolds stress:

$$[R] = 2k \left(\frac{1}{3}[I] + [A] \right) = 2k \left(\frac{1}{3}[I] + [E][\Lambda][E]^T \right) \quad (1)$$

where k is the turbulent kinetic energy which indicates the magnitude of $[R]$; $[I]$ is the second order identity tensor; $[A]$ is the anisotropy tensor; $[E] = [\vec{e}_1, \vec{e}_2, \vec{e}_3]$ and $[\Lambda] = \text{diag}[\tilde{\lambda}_1, \tilde{\lambda}_2, \tilde{\lambda}_3]$ where $\tilde{\lambda}_1 + \tilde{\lambda}_2 + \tilde{\lambda}_3 = 0$ are the orthonormal eigenvectors and the corresponding eigenvalues of $[A]$, respectively, indicating the shape and orientation of $[R]$. The Lumley triangle is thus defined on a plane with the second and third invariants (II and III) of the anisotropy tensor as coordinates, where $\text{II} = (\text{tr}[A])^2 - \text{tr}([A]^2)$ and $\text{III} = \det[A]$.

The realizable turbulence models have demonstrated superior performance in some cases compared to their standard counterpart models that do not guarantee realizability. Interestingly, however, several decades after their development they have not dominated the non-realizable models. Among the handful of standard, most widely used turbulence models (e.g., $k-\varepsilon$ [27], $k-\omega$ SST model [28], and SA model [29]) that are implemented in industrial

¹This is actually the negative of the Reynolds stress [22].

standard CFD packages, none of them are realizable models.

2.2. Realizability in Physics-Based Model-Form Uncertainty Quantification

The past two decades have not seen significant literature on the realizability of turbulence models, partly because the research on RANS model development has been stagnant all together. However, recently the pioneering research of Iaccarino and co-workers [4, 5, 30] on the quantification of model form uncertainties in RANS simulations has revived the interests on Reynolds stresses realizability. Specifically, they performed the decomposition as shown in Eq. (1) and mapped the eigenvalues $\tilde{\lambda}_1$, $\tilde{\lambda}_2$, and $\tilde{\lambda}_3$ to Barycentric coordinates (C_1, C_2, C_3) as follows:

$$C_1 = \tilde{\lambda}_1 - \tilde{\lambda}_2 \quad (2a)$$

$$C_2 = 2(\tilde{\lambda}_2 - \tilde{\lambda}_3) \quad (2b)$$

$$C_3 = 3\tilde{\lambda}_3 + 1. \quad (2c)$$

As illustrated in Fig. 1a, the Barycentric coordinates (C_1, C_2, C_3) of a point indicate portion of areas of the three sub-triangles formed by the point and the edge labeled as C_1 , C_2 , and C_3 , respectively, in the Barycentric triangle. For example, the ratio between the shaded sub-triangle and the entire triangle is C_3 . A point located on the top vertex corresponds to $C_3 = 1$ while a point located on the bottom edge (labeled C_3 in Fig. 1a) has $C_3 = 0$. Therefore, each coordinate ranges from 0 to 1, and they sum to 1 for any point, i.e., $C_1 + C_2 + C_3 = 1$. The three edges labeled C_1 , C_2 and C_3 are opposite to the vertices representing one-component, two-component, and three-component limits of realizable turbulence states. The Barycentric coordinates have clear physical interpretation in that they indicate the componentality (i.e., dimensionality) of the turbulence. For example, the upper corner in Fig. 1a, which corresponds to $C_3 = 1$ or equivalently a Barycentric coordinate of $(0, 0, 1)$, indicates isotropic, fully three-dimensional turbulence. Detailed physical interpretation of the vertices and edges are shown in Fig. 1a. The Barycentric triangle is similar to the Lumley triangle in that it also encloses all realizable turbulence states. Emory et al. [4] estimated the uncertainties in RANS simulations by perturbing the Reynolds stress towards the three limiting states, i.e., the vertices of the Barycentric triangle. This is illustrated in Fig. 1b as squares. Based on their work, Xiao et al. [7] further mapped the Barycentric coordinates to natural coordinates, on which the equilateral triangle is mapped to a unit square. They parameterized the uncertainty space on the natural coordinates and systematically explored the uncertainty space. The samples as obtained in Xiao et al. [7] are illustrated in Fig. 1b, which are in contrast to the three perturbed states of Emory et al. [4].

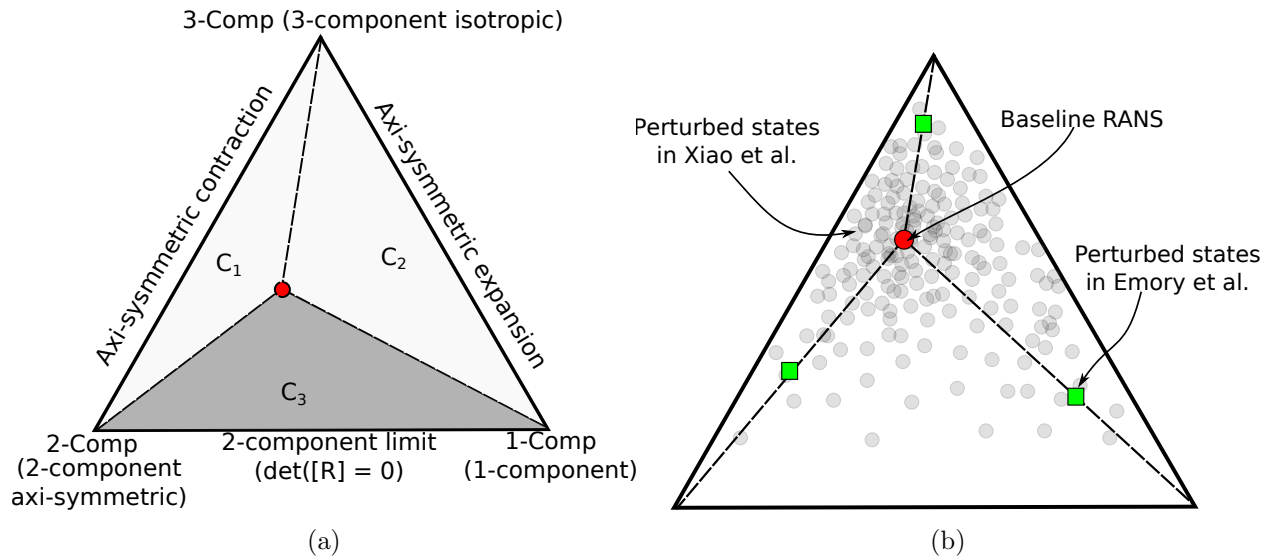


Figure 1: (a) Barycentric triangle as a way of delineating realizable turbulence, its definition and physical interpretation. Elements in the set \mathbb{M}_d^{+0} of positive semidefinite matrices maps to the interior and edges of the triangle, while the set $\mathbb{M}_d^{+0} - \mathbb{M}_d^+$ of singular matrices maps (whose element have zero determinants) maps to the bottom edge. (b) Model-form uncertainty quantification through perturbation of Reynolds stresses within the physically realizable limit enclosed by the Barycentric triangle. The different schemes of Emory et al. [4] and Xiao et al. [7] are shown.

While both Emory et al. [4] and Xiao et al. [7] injected uncertainties only to the magnitude and shape of the Reynolds stress tensor, it is theoretically possible to perturb the orientation as well. This work is not directly concerned with the physics-based approach for uncertainty quantification, but the physics-based parameterization will facilitate interpretations of the samples obtained with the random matrix approach. To this end, a parameterization scheme for the orthonormal eigenvectors $E = [\vec{e}_1, \vec{e}_2, \vec{e}_3]$ is needed. We use the Euler angle with the z - x' - z'' convention to describe the orientation of the Reynolds stress tensor [31]. That is, if a local coordinate system x - y - z spanned by the three eigenvectors of $[R]$ was initially aligned with the global coordinate system (X - Y - Z), the current configuration could be obtained by the following three consecutive intrinsic rotations about the axes of the local coordinate system: (1) a rotation about the z axis by angle φ_1 , (2) a rotation about the x axis by φ_2 , and (3) another rotation about its z axis by φ_3 . Note that the local coordinate axes may change orientations after each rotation.

In summary, the Reynolds stress can be represented with six independent variables with clear physical interpretations. The turbulent kinetic energy k represents its magnitude; the Barycentric coordinates C_1, C_2, C_3 , of which only two are independent, indicate its shape; the Euler angles φ_1, φ_2 and φ_3 represent its orientation. Realizability can be guaranteed by injecting uncertainties in these physical variables, a fact that has been exploited in the physics-based approach for RANS model-form uncertainty quantification investigated in earlier works.

2.3. Mathematical and Physical Interpretations of Realizability

The physics-based approach based on Barycentric triangle as explored by Emory et al. [4] and Xiao et al. [7] certainly has clear advantages. However, it is not the only way to guarantee realizability. Here we claim that an alternative method to guarantee the Reynolds stress realizability in the context of RANS model-form uncertainty quantification is to model $[R]$ as a random matrix defined on the set \mathbb{M}_3^{+0} of positive semidefinite matrices. In other words, we can directly draw $[R]$ from the set \mathbb{M}_3^{+0} and all obtained samples are guaranteed to be realizable Reynolds stresses. To support this claim, we utilize a theorem on the equivalence between the set of positive semidefinite matrices and the set of co-variance matrices (see e.g., [32]). That is, a covariance matrix $[R]$ must be positive semidefinite; conversely, every symmetric positive semi-definite matrix $[R]$ is a covariance matrix. The proof for the first part is straightforward and is thus omitted. However, the proof for the second part is of central importance to the theme of our work, and thus it is reproduced below. We construct a vector $\vec{\mathbf{v}} = [R]^{1/2} \vec{\mathbf{b}}$ with $[R]^{1/2}$ being the symmetric square root of $[R]$ and $\vec{\mathbf{b}}$ has a covariance

of identity matrix, i.e., $\text{Cov}\{\vec{\mathbf{b}}, \vec{\mathbf{b}}\} = [I]$, where $\text{Cov}\{\cdot\}$ indicates covariance. It can be seen that $\text{Cov}\{R^{1/2}\vec{\mathbf{b}}, R^{1/2}\vec{\mathbf{b}}\} = [R]^{1/2} \text{Cov}\{\vec{\mathbf{b}}, \vec{\mathbf{b}}\} [R]^{1/2} = [R]$. For any sample $[R]$ drawn from the set \mathbb{M}_d^{+0} of positive semidefinite matrices, there is a real-valued velocity vector $\vec{\mathbf{v}}$ whose covariance is $[R]$. Recalling the definition and origin of the Reynolds stress realizability described in Section 2.1, it can be seen that the matrix $[R]$ is a realizable Reynolds stress. Therefore, it is concluded that the mathematical constraint that $[R]$ must belong to the set \mathbb{M}_3^{+0} can equally guarantee the realizability of the obtained Reynolds stresses, albeit in a different manner from the physics-based approach. The latter utilized the constraint that the projection of Reynolds stresses must reside in the Barycentric triangle to ensure the Reynolds stress realizability.

We conclude this section with the following three *equivalent* statements on the realizability constraints of the Reynolds stresses:

1. a Reynolds stress must reside within or on the edge of the Lumley triangle or Barycentric triangle after certain transformations [9];
2. a Reynolds stress tensor must be positive semidefinite; and
3. a Reynolds stress tensor must be the covariance matrix of a real-valued vector, i.e., a velocity vector.

The equivalence between realizability and the invariants mapping within Lumley triangle was established by Lumley and Neuman [8] and stated in ref. [22] (pp. 394); the equivalence between the positive semidefinite requirement on the Reynolds stress and the realizability conditions was proved by Schumann [23]. The relation among three statements above is a pivotal element for anchoring the present contribution to the existing literature of turbulence modeling [4, 8, 23]. However, note that the proposed random matrix approach for quantifying RANS model-form uncertainty is fundamentally different from the physics-based approach developed in ref. [7]. The most important difference lies in the fact that in the physics-based approach the user specifies the probability distribution on the physical variables, while in the random matrix approach the maximum entropy principle provides the basis for computing the distribution of the matrices.

3. Random Matrix Approach and Its Implementation

3.1. Probability Model for Reynolds Stress Tensors

Based on the discussions above on the nature of Reynolds stresses, we build a probabilistic model for the Reynolds stress tensors. The development below mostly follow the works of

Soize, Ghanem, and co-workers [e.g., 16, 17].

Using \mathbb{M}_d^s to denote the set of all symmetric matrices, the measure of matrix $[R] \in \mathbb{M}_d^s$ is given as [20]:

$$d[R] = 2^{d(d-1)/4} \prod_{1 \leq i < j \leq d} dR_{ij} \quad (3)$$

where \prod indicates product, R_{ij} are individual element of matrix $[R]$, and dR_{ij} is the Lebesgue measure on the set \mathbb{R} of real numbers. Since Reynolds stresses are rank two tensors, $d = 3$ is implied.

The objective is to define a probability measure $p_{[\mathbf{R}]} : \mathbb{M}_d^{+0} \mapsto \mathbb{R}^+$ on the symmetric matrices set that maps a symmetric, positive semidefinite, second-order random matrix $[\mathbf{R}]$ to a positive number. While such a measure is not unique, in this work we seek a probability density function (PDF) that has the maximum entropy. Specifically, let P_{ad} be the set of all the PDFs from \mathbb{M}_d^{+0} to \mathbb{R}^+ , the maximum entropy principle states that the most non-committal PDF is the one such that all available constraints are satisfied but without introducing any other artificial constraints [18], i.e.,

$$p_{[\mathbf{R}]} = \arg \max_{p \in P_{ad}} S(p) \quad (4)$$

where the measure of entropy $S(p)$ of the PDF p is defined as [16]:

$$S(p) = - \int_{\mathbb{M}_d^{+0}} p([R]) \ln p([R]) d[R] \quad (5)$$

where \ln denotes the natural logarithm.

In the context of RANS-based turbulence modeling, the following constraints should be satisfied by the PDF of Reynolds stress tensors:

1. All realizations $[R]$ of the Reynolds stress $[\mathbf{R}]$ must be physically realizable. This constraint is automatically satisfied by defining $[\mathbf{R}]$ on the set \mathbb{M}_d^{+0} , i.e., $[\mathbf{R}] \in \mathbb{M}_d^{+0}$.
2. Normalization condition for the PDF:

$$\int_{\mathbb{M}_d^{+0}} p_{[\mathbf{R}]}([R]) d[R] = 1, \quad (6)$$

which is self-evident.

3. We assume that a best estimation $[\underline{R}]$ of the unknown Reynolds stress $[\mathbf{R}]$ is available at any location in the field. The estimation can be obtained in advance by performing

a baseline RANS simulation or by incorporating observation data and incorporating prior corrections to the baseline RANS-predicted Reynolds stresses. Without further information, it is reasonable to take the best estimation $[\underline{R}]$ obtained this way as the mean of the true Reynolds stress $[\mathbf{R}]$, with the latter being modeled as a random variable. This constraint is expressed as follows:

$$\mathbb{E}\{[\mathbf{R}]\} = [\underline{R}]. \quad (7)$$

The theories on the maximum distribution of random matrices developed in the earlier works of Soize and co-workers focused primarily on positive definite matrices, but the Reynolds stress tensors of concern in the present application are positive semidefinite only. Although we have claimed that the difference has no practical consequences, we shall still carefully reconcile the differences before utilizing the theories of Soize [16]. In order to obtain a maximum entropy distribution for a positive definite matrix that satisfies the normalization and mean constraints similar to those outlined above, Soize [16] took a two-step approach. Specifically, he first obtained the PDF for a *normalized, positive definite* random matrix $[\mathbf{G}]$ whose mean is the identity matrix $[I]$, i.e., $\mathbb{E}\{[\mathbf{G}]\} = [I]$. The probability distribution for $[\mathbf{G}]$ must also satisfy the maximum entropy condition and the normalization condition in Eq. (6) above. Once such a matrix $[G]$ is obtained, a matrix that satisfies the condition $\mathbb{E}\{[\mathbf{R}]\} = [\underline{R}]$ can be constructed as follows:

$$[\mathbf{R}] = [\underline{L}_R]^T [\mathbf{G}] [\underline{L}_R], \quad (8)$$

where $[\underline{L}_R]$ is an upper triangular matrix with non-negative diagonal entries obtained from the following factorization of the specified mean $[\underline{R}]$, i.e.,

$$[\underline{R}] = [\underline{L}_R]^T [\underline{L}_R]. \quad (9)$$

In the present development, we consider the following two scenarios. (1) When $[R] \in \mathbb{M}_d^+$ is positive definite, the decomposition above is the well-known Cholesky factorization, and the decomposition is unique. Its numerical implementations are available in many standard numerical toolboxes (e.g., Matlab and the numpy library of Python). (2) When $[R] \in \mathbb{M}_d^{+0} \setminus \mathbb{M}_d^+$ is in the subset of singular positive semidefinite matrices, where \setminus indicates set subtraction, it can be proved that the decomposition in the form above still exists with L having non-negative diagonal entries, although the decomposition is no longer unique. Moreover, Cholesky factorization routines for such matrices are still numerically stable if complete pivoting is performed [33]. In practice, we can make it slightly positive definite by

adding a small element to the diagonal entries and thus still use the conventional Cholesky factorization routines.

With the reconciliation above, hereafter we only need to focus on probability distribution of the normalized positive definite matrix $[\mathbf{G}]$ and can thus directly use the results in the earlier works of [20]. By using the classical optimization techniques based on Lagrange multipliers, the probability density function of the random matrix $[\mathbf{G}]$ is obtained as follows [20]:

$$p_{[\mathbf{G}]}([G]) = \mathbb{1}_{\mathbb{M}_d^+}([G]) \times C_G \times \det[G] (d+1)(1-\delta^2)/(2\delta^2) \times \exp\left(-\frac{d+1}{2\delta^2} \text{tr}[G]\right), \quad (10)$$

where $\mathbb{1}_{\mathbb{M}_d^+}([G])$ is an indicator function, i.e., it is one if $[G] \in \mathbb{M}_d^+$ and is zero otherwise. The positive constant C_G is:

$$C_G = \frac{(2\pi)^{-d(d-1)/4} \left(\frac{d+1}{2\delta^2}\right)^{d(d+1)(2\delta^2)^{-1}}}{\prod_{j=1}^d \Gamma\left(\frac{d+1}{2\delta^2} + \frac{1-j}{2}\right)} \quad (11)$$

where $\Gamma(z)$ is gamma function defined by $\Gamma(z) = \int_0^\infty t^{z-1} e^{-t} dt$. The dispersion parameter δ indicates the uncertainty in the random matrix and is defined as:

$$\delta = \left[\frac{1}{d} \mathbb{E}\{\|[G] - [I]\|_F^2\} \right]^{\frac{1}{2}} \quad (12)$$

where $\|\cdot\|_F$ is Frobenius norm, e.g., $\|G\|_F = \sqrt{\text{tr}([G]^T[G])}$. It can be seen that δ is analogous to the variance of a scalar random variable normalized by its mean. It has been shown [16] that

$$0 < \delta < \sqrt{\frac{d+1}{d+5}}, \quad (13)$$

which reduces to $0 < \delta < \sqrt{2}/2$ for $d = 3$. This constraint is related to the positive definiteness of matrix $[\mathbf{G}]$.

The individual elements in the random matrix $[\mathbf{G}]$ are correlated and the same can thus be said for the random matrix $[\mathbf{R}]$. This correlation needs to be accounted for when generating Monte Carlo samples, which can be achieved in a similar way as in sampling from random processes (e.g., Gaussian processes). The sampling method is detailed below.

3.2. Monte Carlo Sampling of Reynolds Stresses at One Point

Soize [16] outlined a Monte Carlo method to sample the probability distribution for random matrix $[\mathbf{R}]$ for a given dispersion parameter δ and mean $[\underline{R}]$. To proceed with

the sampling, the random matrix with identity mean is first represented by its Chelosky factorization:

$$[\mathbf{G}] = [\mathbf{L}]^T[\mathbf{L}], \quad (14)$$

where random matrix $[\mathbf{L}]$ are upper triangular matrices with independent elements. In the procedure, each element \mathbf{L}_{ij} in matrix $[\mathbf{L}]$ is sampled independently with the algorithms below (see Section 5.1 in ref. [34]):

1. The off-diagonal elements \mathbf{L}_{ij} with $i < j$ are obtained from

$$\mathbf{L}_{ij} = \sigma_d \mathbf{w}_{ij}, \quad (15)$$

in which $\sigma_d = \delta \times (d + 1)^{-1/2}$, and \mathbf{w}_{ij} (i.e., \mathbf{w}_{12} , \mathbf{w}_{13} , and \mathbf{w}_{23}) are independent Gaussian random variables with zero mean and unit variance.

2. The diagonal elements are generated as follows:

$$\mathbf{L}_{ii} = \sigma_d \sqrt{2\mathbf{u}_i} \quad \text{with } i = 1, 2, 3 \quad (16)$$

where \mathbf{u}_i is a positive valued gamma random variable with the following probability density function:

$$p(u) = \mathbb{1}_{\mathbb{R}^+}(u) \frac{u^{\frac{d+1}{2\delta^2} + \frac{1-i}{2} - 1} \exp(-u)}{\Gamma\left(\frac{d+1}{2\delta^2} + \frac{1-i}{2}\right)} \quad (17)$$

That is, the i^{th} diagonal term \mathbf{u}_i conforms to gamma distribution with shape parameter $k = (d + 1)/(2\delta^2) + (1 - i)/2$ and scale parameter 1.

3. After obtaining the elements as above, a realization $[L]$ of the random matrix $[\mathbf{L}]$ can be assembled. Subsequently, realizations $[G]$ and $[R]$ for matrices $[\mathbf{G}]$ and $[\mathbf{R}]$, respectively, can be obtained from $[\mathbf{G}] = [\mathbf{L}]^T[\mathbf{L}]$ and $[\mathbf{R}] = [\underline{L}_R]^T[\mathbf{G}][\underline{L}_R]$ as in Eqs. (14) and (8).

3.3. Random Matrix Field Model for Reynolds Stresses

The probability model and the Monte Carlo sampling algorithm described in Sections 3.1 and 3.2 above concerns the Reynolds stress tensor at a single point. An important challenge in the present application is to represent and model the correlation of Reynolds stress at different spatial locations. This feature distinguishes the present contribution from previous applications of random matrix in composite materials models[17] and structural dynamics [21].

In this work we assume that the off-diagonal terms and the square roots of the diagonal terms have the same spatial correlation structures. Gaussian kernel is among the most common choice in the literature, but other kernels such as periodic (e.g., sinusoidal) kernels [18] or exponential kernels [35] have been used as well. The choice of kernel is reflected in the smoothness of the realizations of the random tensor field \mathbf{L} . With the Gaussian kernel used in this work, the correlation between two random variables at two spatial locations x and x' can be written as:

$$\rho_L\{\mathbf{L}_{ij}(x), \mathbf{L}_{ij}(x')\} \equiv \frac{\text{Cov}\{\mathbf{L}_{ij}(x), \mathbf{L}_{ij}(x')\}}{\sigma_{ij}(x)\sigma_{ij}(x')} = \exp\left[-\frac{|x-x'|^2}{l^2}\right] \quad \text{for } i < j \quad (18a)$$

$$\rho_L\{\mathbf{L}_{ii}^2(x), \mathbf{L}_{ii}^2(x')\} \equiv \frac{\text{Cov}\{\mathbf{L}_{ii}^2(x), \mathbf{L}_{ii}^2(x')\}}{\sigma_{ii}(x)\sigma_{ii}(x')} = \exp\left[-\frac{|x-x'|^2}{l^2}\right] \quad x, x' \in \Omega \quad (18b)$$

where Ω is the spatial domain of the flow field. Note that repeated indices *do not* imply summation. $\sigma_{ij}^2(x)$ and $\sigma_{ii}^2(x)$ are the variances of the marginal distributions for the off-diagonal elements $\mathbf{L}_{ij}(x)$ and the square of the diagonal elements $\mathbf{L}_{ii}^2(x)$, respectively. That is, $\text{var}\{\mathbf{L}_{ij}(x)\} = \sigma_{ij}^2(x)$ and $\text{var}\{\mathbf{L}_{ii}^2(x)\} = \sigma_{ii}^2(x)$, the expression of which will be given in Eqs. (21) and (25), respectively. ρ_L is the correlation kernel, $|\cdot|$ is the Euclidean norm of vectors, and l is the correlation length scale of the stochastic process. We emphasize that the correlations above are between *the same element at different locations* x and x' , and that the random variables \mathbf{L}_{11} , \mathbf{L}_{22} , \mathbf{L}_{33} , \mathbf{L}_{12} , \mathbf{L}_{13} , and \mathbf{L}_{23} , which are different elements of the matrix $[\mathbf{L}]$, are still independent of each other as pointed out above.

With the correlation model defined in Eq. (18) for the elements of matrix $[\mathbf{L}]$, the random variables used to generate L_{ij} in Eqs. (15) and (16) can be generalized to random fields. First, it is straightforward to generalize the Gaussian random variable \mathbf{w}_{ij} to a Gaussian random field (also referred to as Gaussian process),

$$\mathbf{L}_{ij}(x) = \sigma_d(x)\mathbf{w}_{ij}(x), \quad (19)$$

where $\mathbf{L}_{ij}(x)$ and $\mathbf{w}_{ij}(x)$ are random fields indexed by the spatial coordinate x , and

$$\sigma_d(x) = \delta(x) (d+1)^{-1/2} \quad (20)$$

is a spatially varying field specifying the standard deviation of the marginal distribution of $L_{ij}(x)$ at location x . Simple algebra shows that if we choose $\mathbf{w}_{ij}(x) \sim \mathcal{GP}(0, K)$ as the Gaussian process with covariance kernel $K(x, x') = \exp[-(|x-x'|^2)/l^2]$ as in Eq. (18), then

$$\sigma_{ij}(x) = \sigma_d(x) = \frac{\delta(x)}{\sqrt{d+1}}, \quad \text{or equivalently} \quad \sigma_{ij}^2(x) = \frac{\delta^2(x)}{d+1}. \quad (21)$$

The Gaussian processes $\mathbf{w}_{ij}(x)$ can be expressed by using the Karhunen–Loeve (KL) expansion, which can be written as follows when truncated to N_{KL} terms:

$$\mathbf{w}_{ij}(x) = \sum_{\alpha=1}^{N_{\text{KL}}} \sqrt{\lambda_{\alpha}} \phi_{\alpha}(x) \boldsymbol{\omega}_{\alpha} \quad (22)$$

where $\boldsymbol{\omega}_{\alpha} \sim \mathbf{N}(0, 1)$ with $\alpha = 1, \dots, N_{\text{KL}}$ being the standard Gaussian random variables; λ_{α} and $\phi_{\alpha}(x)$ are the eigenvalue and the corresponding eigenfunction for the α^{th} mode obtained by solving the Fredholm integral equation [36]:

$$\int_{\Omega} \rho(x, x') \phi(x') dx' = \lambda \phi(x), \quad (23)$$

where Ω is the spatial domain of the flow as defined above.

Remarks on using nonstationary and anisotropic kernels to reflect the structure of the flow field. Non-stationarity and anisotropy in the Gaussian process $\mathbf{w}(x)$ can be achieved by using spatially varying and/or anisotropic length scale $l(x)$, which depends on the characteristics of the mean flow. For example, for a nonstationary Gaussian process, the length scale l in Eq. (18) can be written as $l = \sqrt{l(x)l(x')}$ following ref. [37]. As such, the physical structure of the flow field is encoded in the Karhunen–Loeve basis functions. It is also desirable to specify different variance $\sigma_{ij}(x)$ at different locations. For example, in regions with flow separation and pressure gradient, the Boussinesq assumptions are violated and thus most RANS models have poor performance. Consequently, the variance $\sigma_{ij}(x)$ should be larger in these regions, which can be achieved by specifying the dispersion parameter $\delta(x)$ to depend on the location x .

The sampling algorithm for the random variables of the diagonal terms in Eq. (16) can be similarly generalized to random fields as follows:

$$\mathbf{L}_{ii}(x) = \sigma_d(x) \sqrt{2 \mathbf{u}_i(x)}, \quad (24)$$

where $\sigma_d(x)$ is defined the same as above. Recall the facts that $\mathbf{u}_i(x)$ has a gamma distribution with shape parameter $k = (d+1)/(2\delta^2) + (1-i)/2$ and that $\text{Var}\{\mathbf{u}_i\} = k$. Substituting Eq. (20) into Eq. (24) and using the two facts above, after some algebra one can show that

$$\sigma_{ii}^2 \equiv \text{Var}\{\mathbf{L}_{ii}^2\} = 4\sigma_d^4 \text{Var}\{\mathbf{u}_i\} = \frac{2\delta^2}{d+1} + \frac{2\delta^4}{(d+1)^2} \times (1-i) \quad \text{for } i = 1, 2, 3, \quad (25)$$

where $d = 3$, and the spatial dependence of all other variables are omitted for notational brevity. However, since $\mathbf{u}_i(x)$ are random fields with gamma marginal distributions, they

are not straightforward to synthesize. Although the KL expansion above can still be used to represent the random field $\mathbf{u}_i(x)$, the corresponding coefficients obtained from the expansion are neither independent nor Gaussian. To overcome this difficulty, we follow the procedure in ref. [35] and express the gamma random variables \mathbf{u}_i at any location x with polynomial chaos expansion:

$$\begin{aligned} \mathbf{u}(x) &= \sum_{\beta=0}^{N_p} U_\beta(x) \Psi_\beta(\mathbf{w}(x)) \\ &= U_0 + U_1 \mathbf{w}(x) + U_2(\mathbf{w}^2(x) - 1) + U_3(\mathbf{w}^3(x) - 3\mathbf{w}(x)) + U_4(\mathbf{w}^4(x) - 6\mathbf{w}^2(x) + 3) + \dots \end{aligned} \quad (26)$$

where N_p is the order of polynomial expansion; for a given x , $\Psi_\beta(\mathbf{w}(x))$ are the Hermite polynomials in standard Gaussian random variable $\mathbf{w}(x)$, with the first four terms explicitly written as above; U_β is the coefficients for the β^{th} polynomial, for which the spatial index x has been omitted for brevity. The coefficients can be obtained from orthogonality conditions with respect to the Gaussian measure [38]:

$$U_\beta = \frac{\langle \mathbf{u} \Psi_\beta \rangle}{\langle \Psi_\beta^2 \rangle} = \frac{1}{\langle \Psi_\beta^2 \rangle} \int_{-\infty}^{\infty} F_{\mathbf{u}}^{-1}[F_{\mathbf{w}}(w)] \Psi_\beta(w) p_{\mathbf{w}}(w) dw \quad (27)$$

where $\langle \Psi_\beta^2 \rangle$ is the variance of i^{th} order polynomial of standard Gaussian random variable; $F_{\mathbf{w}}(\mathbf{w})$ and $p_{\mathbf{w}}(\mathbf{w})$ are the cumulative distribution function (CDF) and PDF, respectively, of the standard Gaussian variable; $F_{\mathbf{u}}$ and $F_{\mathbf{u}}^{-1}$ are the CDF and its inverse, respectively, of random variable \mathbf{u} . As indicated previously, Eq. (27) is evaluated for each x with $\mathbf{w}(x)$ being a standard Gaussian variable.

Sakamoto and Ghanem [35] have derived the relation between spatial correlation of the non-Gaussian field $\mathbf{u}(x)$, i.e., $\rho_u\{\mathbf{u}(x), \mathbf{u}(x')\}$ and the correlation $\rho_w\{\mathbf{w}(x), \mathbf{w}(x')\}$ of the Gaussian random field $\mathbf{w}(x)$ used in its polynomial chaos representation. This is achieved by substituting Eq. (26) into the definition of covariance. They further showed that the following approximation yields very good accuracy:

$$\rho_u\{\mathbf{u}(x), \mathbf{u}(x')\} \approx \rho_w\{\mathbf{w}(x), \mathbf{w}(x')\}. \quad (28)$$

We have verified that the two are indeed approximately equal based on the generated samples. This approximation above is what we shall use in our work. Therefore, given the correlation structure of field \mathbf{u}_i , an approximation of the kernel $\rho_w\{\mathbf{w}(x), \mathbf{w}(x')\}$ is obtained, which can be used in the KL expansion to find the eigenmodes and further synthesize the Gaussian random fields \mathbf{w}_{ii} . Finally, the non-Gaussian random field $\mathbf{u}_i(x)$ can be obtained by reconstructing from the polynomial chaos based on Eq. (26) at each location $x \in \Omega$.

3.4. Monte Carlo Sampling of Reynolds Stress Fields

Based on the development above, the algorithm of Monte Carlo sampling of Reynolds stress field can be performed as follows:

1. Draw independent samples ω_α from the standard Gaussian distribution $\mathbf{N}(0, 1)$ with $\alpha = 1, \dots, N_{\text{KL}}$.
2. Use the KL expansion in Eq. (22) to reconstruct a Gaussian random field $w(x)$ with λ_α and $\phi_\alpha(x)$ obtained from solving Eq. (23).
3. Repeat steps 1–2 above six times to obtain six independent realizations of Gaussian random fields $w_{12}(x)$, $w_{13}(x)$, $w_{23}(x)$, $w_{11}(x)$, $w_{22}(x)$, and $w_{33}(x)$. The first three will be used to synthesize the off-diagonal elements $L_{12}(x)$, $L_{13}(x)$, and $L_{23}(x)$, respectively, and the last three for the diagonal elements $L_{11}(x)$, $L_{22}(x)$, and $L_{33}(x)$, respectively.

Remark on the choice of KL modes for the representation of the six Gaussian random fields. In this work the same KL modes ϕ_α and eigenvalues λ_α are used for generating all six realizations $w(x)$ of Gaussian random fields above. This is a modeling choice made for simplicity and also for the lack of prior knowledge to justify otherwise. However, in cases where it is desirable to use a different number N_{KL} of modes or even a different kernel $K(x, x')$ for each field, it can be achieved in a straightforward manner as well.

4. Synthesize off-diagonal elements based on Eq. (19).
5. Reconstruct the random fields $\mathbf{u}_1(x)$, $\mathbf{u}_2(x)$, and $\mathbf{u}_3(x)$ based on the polynomial chaos expansion in Eq. (26) and further obtain the fields $\mathbf{L}_{11}(x)$, $\mathbf{L}_{22}(x)$, and $\mathbf{L}_{33}(x)$ based on Eq. (24).

3.5. Considerations in Numerical Implementation

For clarity we outline the complete algorithm of sampling of Reynolds stress fields and the propagation to velocities and other QoIs in [Appendix A](#). Remarks are made below on computational considerations in implementing the proposed algorithm.

In the expansions described in Sections 3.2 and 3.3, the Cholesky factorization of the Reynolds stress, the polynomial chaos expansion of the marginal distribution of the gamma random variable \mathbf{u}_i , and the KL expansion of the Gaussian random field all need to be performed on a mesh. Theoretically, they all can be performed on the RANS simulation mesh. However, this choice would lead to unnecessarily high computational costs. The RANS

mesh is designed to resolve the flow field features. Usually it is refined in the near-wall region to resolve the boundary layer. On the other hand, the mesh for the KL expansion only needs to resolve the length scale of the correlation, i.e., the field $l(x)$. Finally, the mesh needed for the polynomial chaos expansion need to resolve the variation of the dispersion parameter $\delta(x)$ field. If the dispersion is constant throughout the domain, one polynomial chaos expansion is sufficient. Therefore, the three expansions and the corresponding reconstructions below are performed on separate meshes, which are referred to as RANS mesh, PCE mesh, and KL mesh, respectively. Interpolations are needed when performing operations on fields based on different meshes. For example, in Eq. (26) where the gamma field is reconstructed from the coefficients $U_\beta(x)$ and the Hermite polynomials in the Gaussian random field $\mathbf{w}(x)$, the coefficients are based on the PCE mesh while the Gaussian random field is based on the KL mesh. An interpolation of the coefficients $U_\beta(x)$ from the PCE mesh to the KL mesh is thus needed. The obtained gamma fields \mathbf{u}_i , the diagonal terms $\mathbf{L}_{ii}(x)$, and the matrix $\mathbf{G}(x)$ are thus based on the KL mesh as well. Similarly, therefore, when the Reynolds stress is reconstructed from $[\mathbf{R}] = [\underline{L}_R]^T[\mathbf{G}][\underline{L}_R]$, the matrix $[\mathbf{G}]$ is first interpolated from the KL mesh to the RANS mesh, so that the obtained Reynolds stress realization $[R]$ can be used in the RANS simulation.

4. Numerical Results

In this section we use the flow over periodic hills at Reynolds number $Re = 2800$ to demonstrate the proposed model-form uncertainty quantification scheme for RANS simulations. The computational domain is shown in Fig. 2, where all dimensions are normalized with the crest height H . The Reynolds number Re is based on the crest height H and bulk velocity U_b at the crest. Periodic boundary conditions are applied at the boundaries in the streamwise (x) direction while non-slip boundary conditions are imposed at the walls. The spanwise direction is not considered since the mean flow is two-dimensional. Benchmark data from direct numerical simulations are used to compare with the sampled Reynolds stresses and the velocities obtained by propagating the Reynolds stresses through the RANS solver.

4.1. Cases Setup

The dispersion parameter is a critical free parameter in the uncertainty quantification scheme. The specification of δ is constrained by requirement $0 < \delta < \sqrt{2}/2$ obtained from Eq. (13) and guided by the subjective belief of the user on the uncertainty in the Reynolds stresses, i.e., larger δ indicates larger uncertainties. We investigate three cases with different

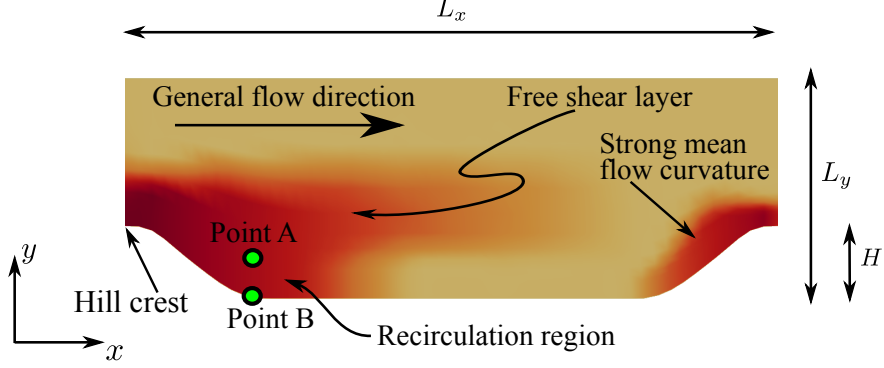


Figure 2: Domain shape for the flow in the channel with periodic hills. The x -, y - and z -coordinates are aligned with the streamwise, wall-normal, and spanwise directions, respectively. All dimensions are normalized by H with $L_x/H = 9$ and $L_y/H = 3.036$. The contour shows the dispersion parameter $\delta(x)$, where darker color denotes larger variance. Two typical points A and B are annotated in the figure.

choices of dispersion parameters: (1) a small dispersion parameter $\delta = 0.2$, (2) a large dispersion parameter $\delta = 0.6$, and (3) a spatially varying $\delta(x)$ field as specified by the color (or grey scale) contour shown Fig. 2. A spatially varying $\delta(x)$ allows the user to encode empirical knowledge about the turbulence model and/or the flow of concern into the prior distribution of Reynolds stresses. For example, in the flow over periodic hills studied here, the underlying Boussinesq assumption is violated in the regions with recirculation, non-parallel free-shear, or strong mean flow curvature (see annotations in Fig. 2). Consequently, these regions are particularly problematic for eddy viscosity models (including the k - ϵ model used in this work). Hence, relatively large dispersion parameters are specified in these regions compared to other regions to reflect the lack of confidence on the model. This is similar to the practice of specifying spatially varying variance fields when injecting uncertainties to the physics-based quantities (magnitude and shape of the Reynolds stress) in Xiao et al. [7]. On the other hand, it is also possible to use maximum likelihood estimation to obtain a dispersion parameter $\delta(x)$ field if some measurement data of Reynolds stresses are available, but this approach is not explored in the present work.

For Cases 1 and 2 with constant dispersion parameters in the domain, the marginal distribution of random matrix $[\mathbf{G}]$ is the same at all locations. Therefore, the polynomial chaos expansion needs to be performed only once. That is, the expansion coefficients U_β in Eq. (27) is spatially uniform. Hence, a PCE mesh is not needed. For Case 3 with a spatially varying $\delta(x)$, a coarse PCE mesh of 15×10 cells is used. In all three cases, the marginal

distribution of the diagonal terms are only weakly non-Gaussian, and thus a third order polynomial expansion is found to be sufficient. In the KL expansion, we used 30 modes, allowing 90% of the variance to be captured. Since the RANS mesh is rather small with only 3000 cells, the KL expansion is performed on the same mesh. In the correlation kernel we used an anisotropic yet spatially uniform length scale ($l_x/H = 2$ and $l_y/H = 1$) to reflect the anisotropy of the flow. The specific numbers are chosen based on the approximate length scale of the mean flow. We use 1000 samples to adequately represent the prior distribution of the Reynolds stresses. To limit the computational cost of the RANS simulations, only 100 of the 1000 samples are randomly selected to propagate to the velocities. The computational parameters discussed above are summarized in Table 1.

Table 1: Mesh and computational parameters used in the flow over periodic hills.

Parameters	Case 1	Case 2	Case 3
dispersion parameter $\delta(x)$	0.2	0.6	0.16–0.65 ^(a)
nature of $\delta(x)$	uniform	uniform	nonuniform
PCE mesh	–	–	15×10
order of polynomial expansion (N_p)	3		
KL mesh	50×30		
RANS mesh	50×30		
number of KL modes N_{KL}	30		
correlation length scales ^(b)	$l_x/H = 2, l_y/H = 1$		
number of Reynolds stress samples	1000		
number of velocity propagation samples	100		

(a) Spatial contour of $\delta(x)$ is shown in Fig. 2.

(b) See Eq. (22)

4.2. Results and Interpretations

As discussed above, 1000 samples of Reynolds stress random field $[\mathbf{R}](x)$ are drawn by using the algorithm described in Section 3.4. An additional challenge is the visualization, validation, and interpretation of the sampled Reynolds stress fields, because in general it is not straightforward to interpret the state of the turbulence from their individual components. To facilitate physical interpretation, in all three cases we map the sampled Reynolds stresses to the six independent physical dimensions with the scheme described in Section 2.2, i.e., the

magnitude k of Reynolds stress tensor, its shape (expressed in Barycentric coordinates C_1 , C_2 , and C_3), and the Euler angles (φ_1 , φ_2 , and φ_3) of its eigenvectors. The scattering of the samples in the Barycentric triangle can be obtained from their Barycentric coordinates, and the probability density functions for all the quantities can be estimated from the samples with a given kernel.

The samples obtained in Case 1 (with $\delta = 0.2$) and Case 2 (with $\delta = 0.6$) are first analyzed by visualizing the scatter plots in the Barycentric triangle, the associated probability density contours, and the marginal distributions of the physical variables (e.g., C_3 , k , and φ_3) for two typical points: (1) point A located at $x/H = 2.0$ and $y/H = 0.5$ and (2) point B located at $x/H = 2.0$ and $y/H = 0.01$. Point A is a generic point in the recirculation region, and point B is a near-wall point with two-dimensional turbulence representing limiting states. The locations of the two points in the domain are indicated in Fig. 2 and in the insets of Figs. 3 and 5.

The scatter plots for the Reynolds stress samples at point A are shown in Figs. 3a and 3b for Cases 1 and 2, respectively. Since this is a generic point, the Reynolds stress state predicted in the baseline simulation is projected to the interior of the Barycentric triangle. While the truth state given by the benchmark simulation is also located in the interior of the triangle, it is further towards the bottom edge, i.e., the two-component limit (see Fig. 1a). Note that the points located on the edges and vertices correspond to limiting states as illustrated in Fig. 1a. In both cases the samples are scattered around the baseline state, suggesting that perturbations introduced in the set \mathbb{M}_d^{+0} about the baseline are still scattered around the corresponding baseline results in the Barycentric triangle. However, the two cases exhibit two notable differences. First, the scattering in Case 2 is much larger than that in Case 1, which is a direct consequence of the larger dispersion parameter ($\delta = 0.6$) compared to that in Case 1 ($\delta = 0.2$). Second, the sample mean deviates significantly from the baseline in Case 2 while they agree quite well in Case 1. This is an interesting observation. Recall that the probability distribution in Eq. (4) is derived under the constraint $\mathbb{E}\{\mathbf{R}\} = \underline{R}$ given in Eq. (7), which implies that the mean of the sample Reynolds stresses should be the baseline prediction assuming the number of samples is large enough. We have verified that the constraint is indeed satisfied and that the sampling error is negligible with the chosen sample number 1000. Therefore, we can see that the mean is not preserved during the projection from the Reynolds stress space to the Barycentric coordinates. This is due to the constraints imposed by the positive definiteness of the Reynolds stress tensor, which manifest itself as the edge boundaries of the Barycentric triangle. When the perturbation

is small relative to the distance of the baseline state to the boundaries, as is the situation in Case 1, the perturbation does not “feel” the constraints. Consequently, the sample mean and the baseline result are approximately the same. In contrast, when the perturbation is large compared to the distance between the baseline and one of the boundaries, the constraint comes into play, leading to appreciable deviations between the sample mean and the baseline. This is better illustrated with the probability density contours in Figs. 3c and 3d for Cases 1 and 2, respectively. The contours in Fig. 3c are approximately elliptic showing little influence from the boundaries. On the other hand, the contours in Figs. 3d clearly follow the three edges at the boundary and displays a triangular shape overall. Since no samples fall outside the Barycentric triangle as can be seen from the scatter plots in both cases, the observation also verified the claim that the random matrix based approach proposed in this work is capable of ensuring Reynolds stress realizability.

To further examine the probability distribution of the Reynolds stress samples, in Fig. 4 we present the discrepancies ΔC_3 , $\Delta\varphi_3$, $\Delta \ln k$ between the sampled and the baseline Reynolds stress for point A. Perturbations on the other physical quantities (e.g., the other Barycentric coordinates ΔC_1 and ΔC_2) have similar characteristics to ΔC_3 presented here and thus are omitted for brevity. Similarly, perturbations $\Delta\varphi_1$ and $\Delta\varphi_2$ for the Euler angles φ_1 and φ_2 are omitted as well. Xiao et al. [7] introduced uncertainties to the predicted Reynolds stresses by modeling the discrepancies in shape and magnitude of the Reynolds stress as Gaussian random fields. It is illustrative to compare the discrepancies above (which are obtained from samples directly drawn in \mathbb{M}_d^{+0}) to the corresponding Gaussian distributions having the same mean and variance as those of the samples. The comparison is performed in Fig. 4, where the PDFs of the Gaussian distributions obtained in this way are presented along with those estimated from samples. It can be seen that in Case 1 the distributions for all three discrepancy quantities ΔC_3 , $\Delta\varphi_3$, $\Delta \ln k$ are rather close to the corresponding Gaussian distributions. In contrast, the corresponding distributions in Case 2 deviate significantly from the Gaussian distributions. It is also noted that the sample mean (denoted in vertical dashed lines; same hereafter) of ΔC_3 deviate slightly from zero in Case 1 but significantly from zero in Case 2, which is consistent with the earlier observations from Figs. 3a and 3b. However, the sample means for $\Delta\varphi_3$ and $\Delta \ln k$ are zero for both Case 1 and Case 2, despite the fact that the sample distribution are non-Gaussian for Case 2. This can be explained by the fact that there are no physical constraints on $\ln k$ or φ (except for the range $[-\pi, \pi]$ specified in the definition). This is in contrast to C_3 , which is bounded in $[0, 1]$. Notably, Figs. 4e and 4f seem to suggest that k (which is the turbulent kinetic energy defined as $\frac{1}{2} \text{tr}([R])$)

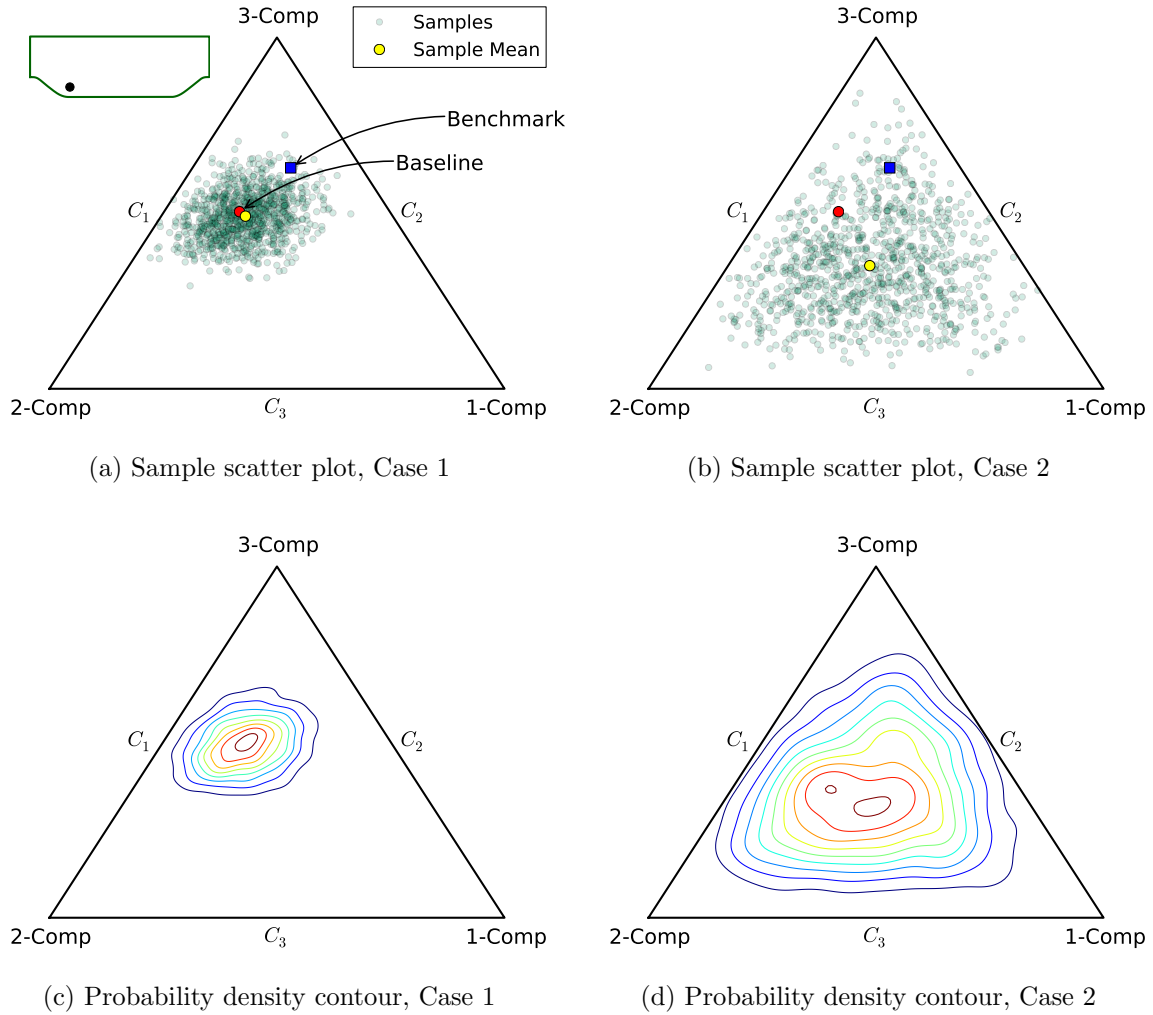
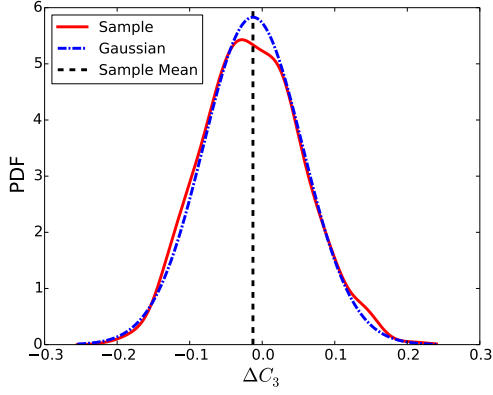


Figure 3: Scatter plots (panels a and b) and probability density contours (panels c and d) of the Reynolds stress samples projected to the Barycentric coordinates for point A ($x/H = 2.0, y/H = 0.5$) located in the recirculation region. Case 1 ($\delta = 0.2$) and Case 2 ($\delta = 0.6$) are compared.

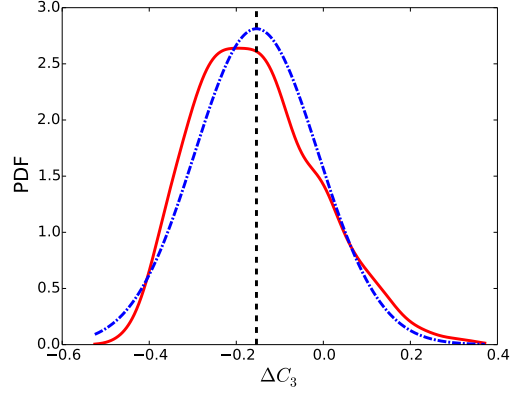
approximately follows a log-normal distribution. This could be related to the term with exponential of $-\text{tr}[G]$ in Eq. (10). Soize [16] also gave the joint distribution of the random eigenvalues of $[\mathbf{R}]$ (see Eq. (64) therein), which theoretically can be marginalized to yield the analytical distribution of k . The analytical expression is, however, extremely complicated and is not pursued in the present work.

It is also of interest to see the probability distribution of the Reynolds stress at a near-wall location with limiting-state turbulence. Therefore, similar to Figs. 3 and 4, the scatter plots and distribution of physical variable are presented in Figs. 5 and 6, respectively, for point B located very close to the bottom wall (at $x/H = 2.0$ and $y/H = 0.01$). The true Reynolds stress at this point is two dimensional, and thus it is located right on the bottom edge of the Barycentric triangle ($C_3 = 0$) as indicated in Figs. 5a and 5b. Recall that C_3 indicates the degree of isotropy (three-dimensionality) of the turbulence. Hence, $C_3 = 0$ indicates that the turbulence is far from isotropic (in fact, it is two-dimensional), which is because the blocking of the wall suppressed almost all fluctuations in wall-normal direction. A standard eddy viscosity model, on the contrary, would predict a nearly isotropic turbulence state with $C_3 = 1$, located near the top vertex of the Barycentric triangle (indicated as dark/red filled circles). The scatter plots corresponding to Cases 1 and 2 are shown in Figs. 5a and 5b, and the corresponding probability density contours are presented in Figs. 5c and 5d. It can be seen that the sample distributions are influenced by the constraints in both cases, since the baseline state is located right next to the boundaries. Moreover, the difference between the sample mean and the baseline are large in both cases, which is also attributed to the constraints as discussed above. The distributions of ΔC_3 , $\Delta \varphi_3$, and $\Delta \ln k$ are presented in Figure 6. For both Cases 1 and 2, the sample distributions of ΔC_3 and $\Delta \varphi_3$ deviate significantly from Gaussian, while the distribution of k is still quite close to log-normal.

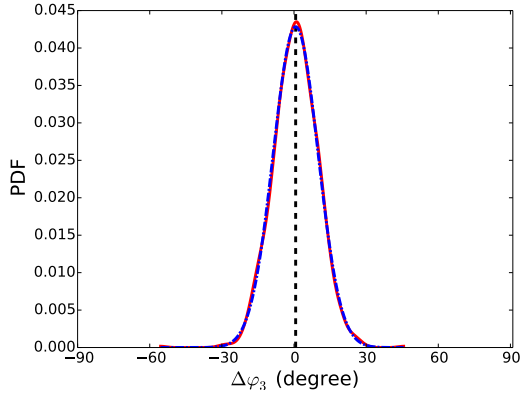
The analysis above focused on the marginal distributions of the Reynolds stresses at two representative locations with a generic and a limiting state turbulence state. Since the Reynolds stress is modeled as a random matrix field, we present the turbulent shear stress R_{12} and the turbulent kinetic energy k in Figs. 7 and 8, respectively. These two quantities are the most relevant for the flow over period hills investigated here. The samples at eight streamwise locations $x/H = 1, 2, \dots, 8$ along with the benchmark and the baseline results. The geometry of the physical domain is also plotted to facilitate visualization. The sample mean profiles coincide with the baselines in most regions for all cases, and thus they are omitted to avoid cluttering. This is in contrast to the deviation of the sample means from the baseline results in the Barycentric triangle as observed in Figs. 3 and 5 for the same



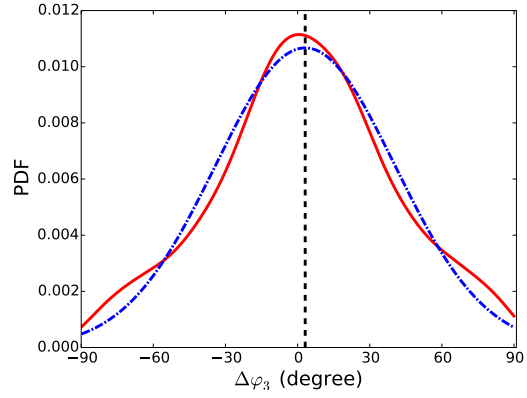
(a) Distribution of ΔC_3 , Case 1



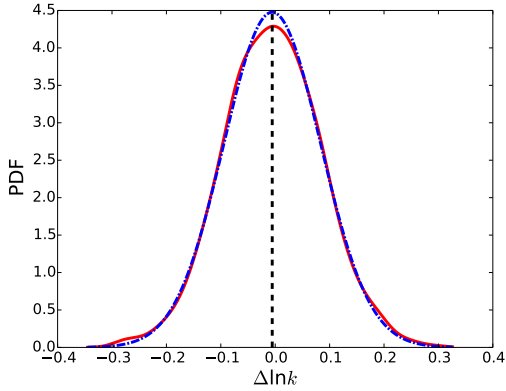
(b) Distribution of ΔC_3 for Case 2



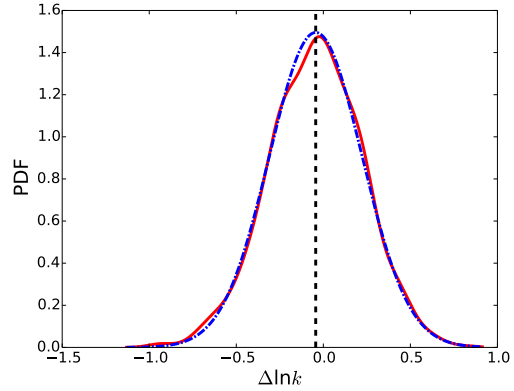
(c) Distribution of $\Delta\varphi_3$ for Case 1



(d) Distribution of $\Delta\varphi_3$ for Case 2



(e) Distribution $\Delta \ln k$ for Case 1



(f) Distribution $\Delta \ln k$ for Case 2

Figure 4: Distributions of the perturbations (ΔC_3 , $\Delta\varphi_3$, and $\Delta \ln k$) in the physical variables for point A ($x/H = 2.0, y/H = 0.5$) located in the recirculation region. The distributions for Case 1 ($\delta = 0.2$) and Case 2 ($\delta = 0.6$) are compared.

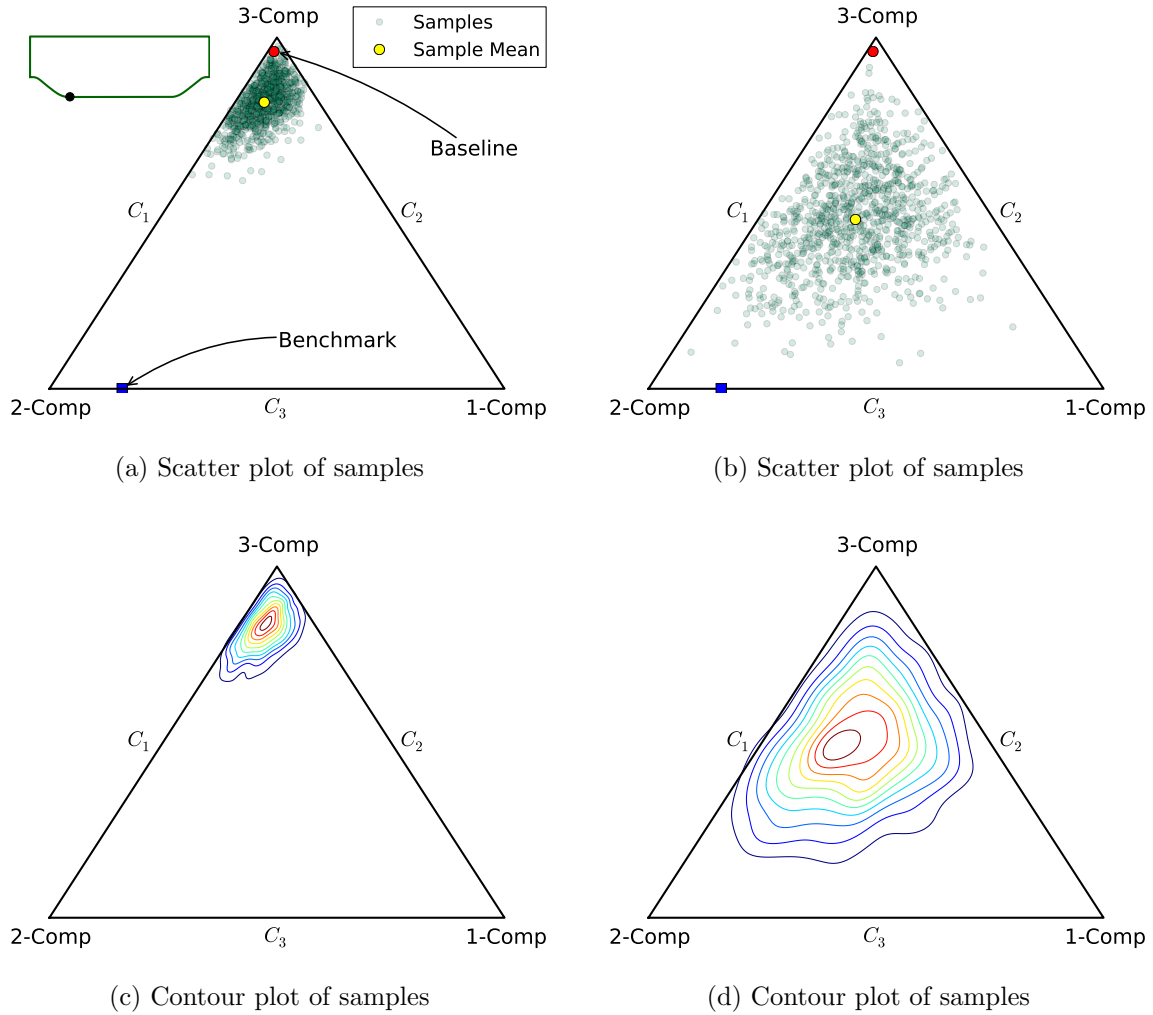


Figure 5: Scatter plots (panels a and b) and probability density contours (panels c and d) of the Reynolds stress samples projected to the Barycentric coordinates for point B ($x/H = 2.0, y/H = 0.01$) located in the recirculation region. Case 1 ($\delta = 0.2$) and Case 2 ($\delta = 0.6$) are compared.

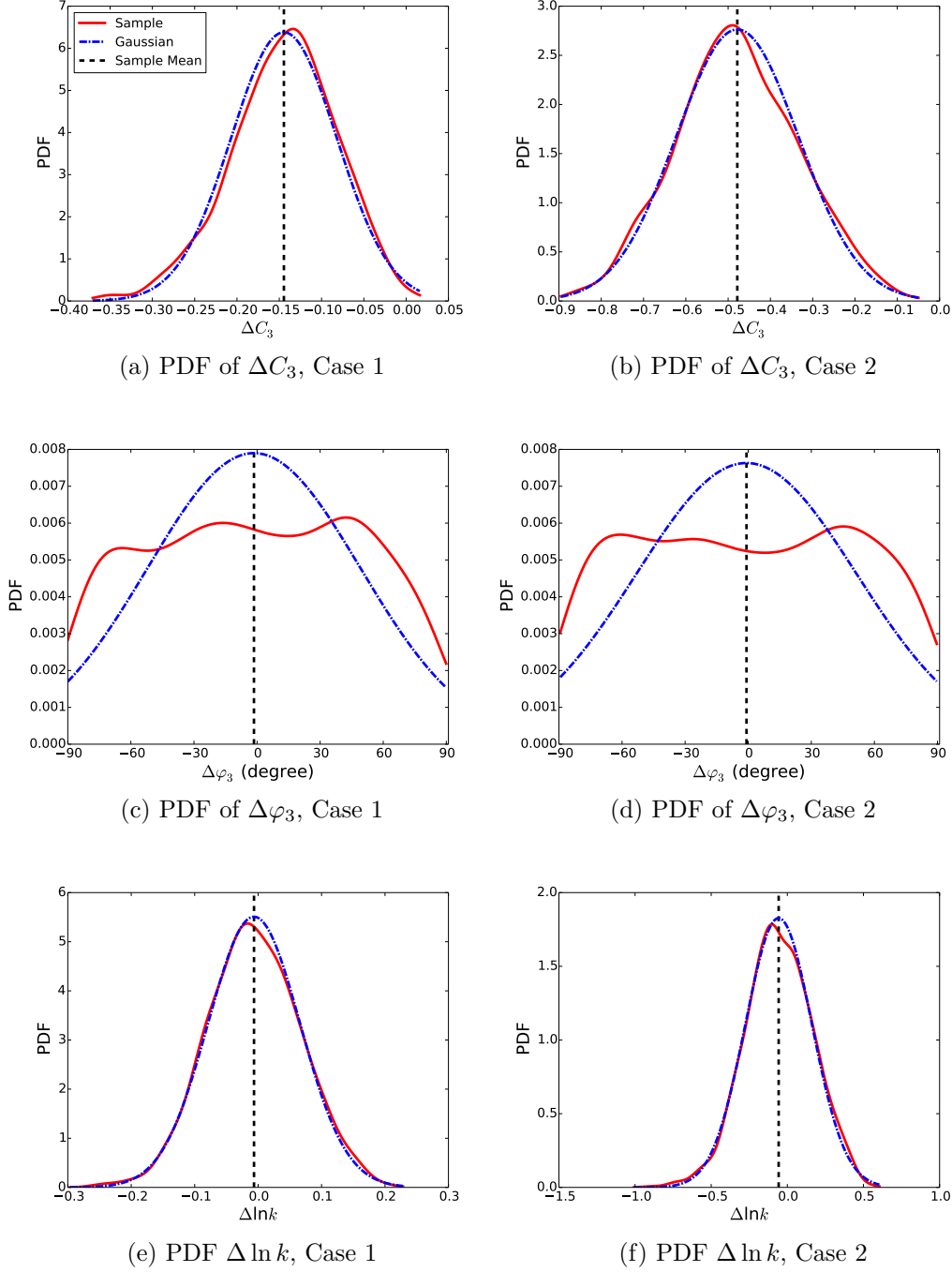


Figure 6: Probability density functions (PDF) of the perturbations (ΔC_3 , $\Delta\varphi_3$, and $\Delta \ln k$) in the physical variables for point B ($x/H = 2.0, y/H = 0.01$) located in the near-wall region. The PDFs for Case 1 ($\delta = 0.2$) and Case 2 ($\delta = 0.6$) are compared.

cases.

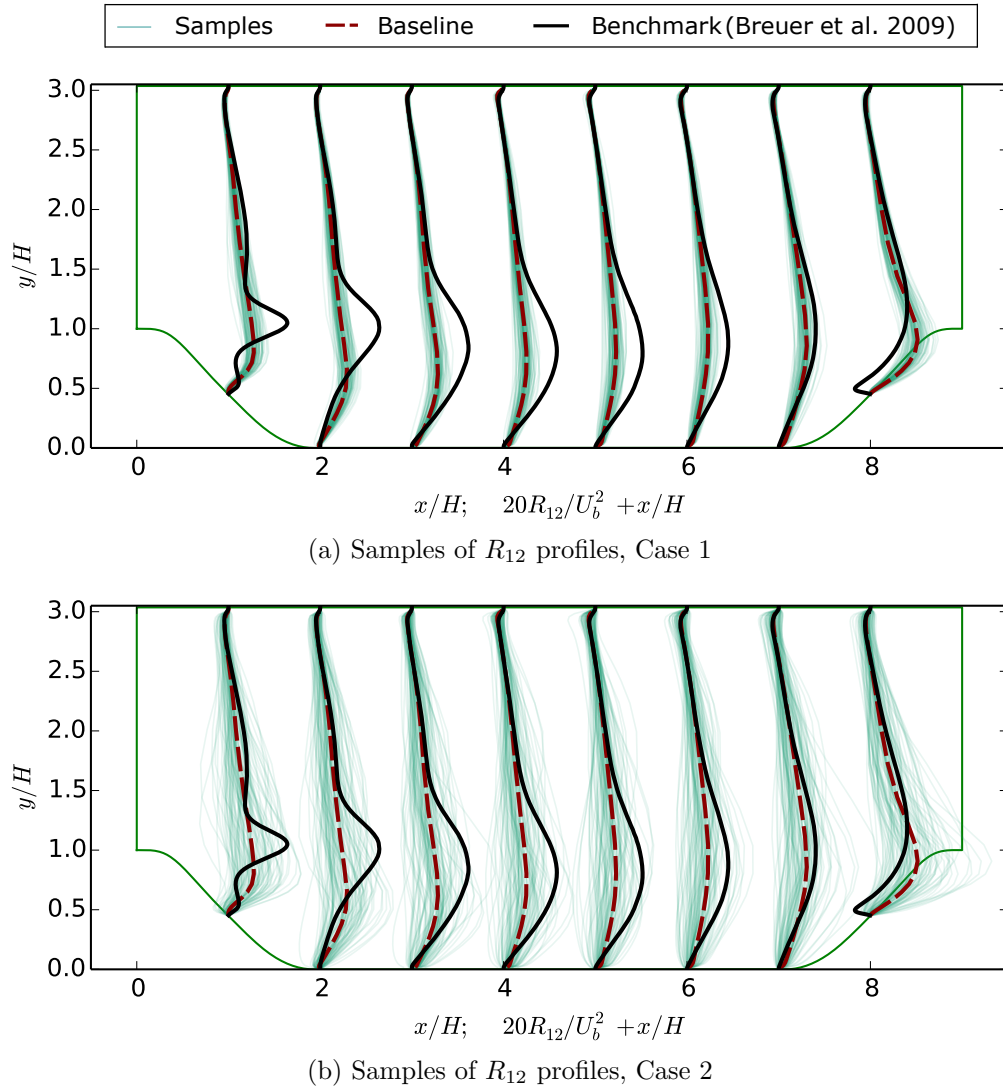
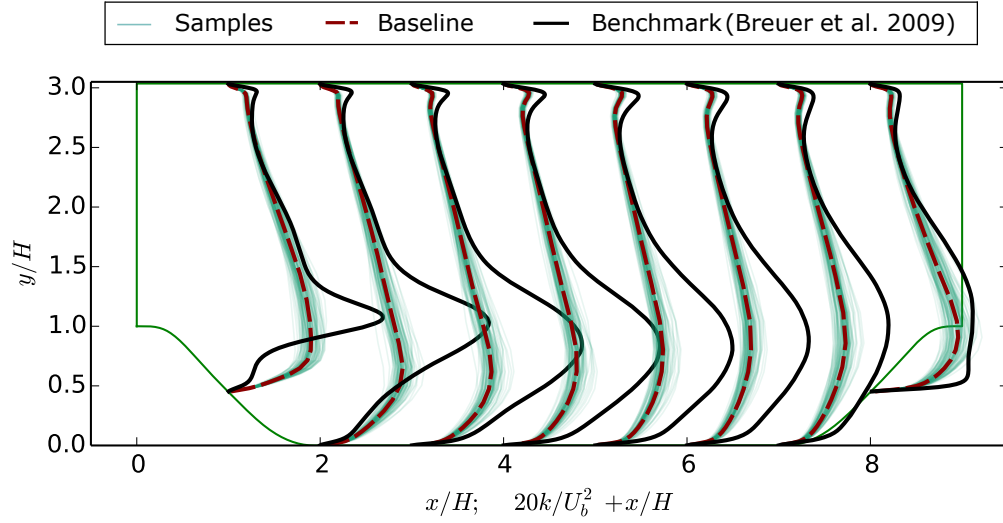
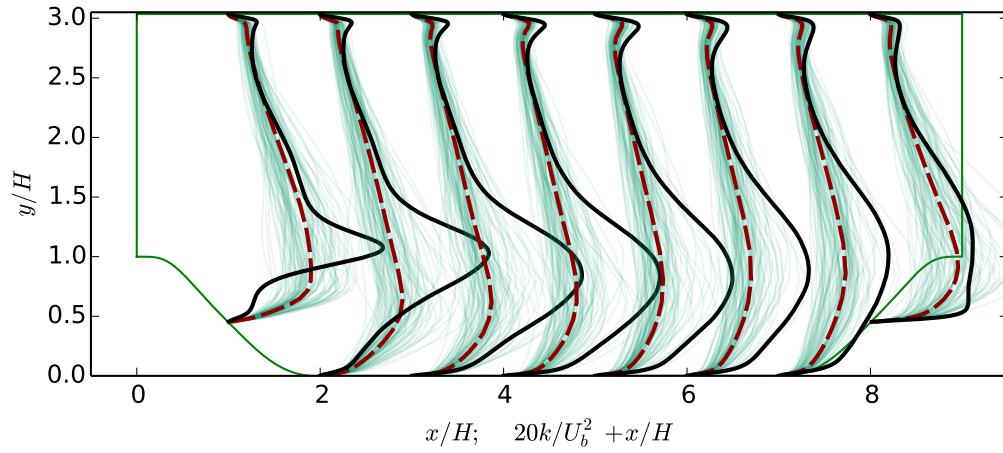


Figure 7: Comparison sample profiles R_{12} for Case 1 and Case 2. The profiles are shown at eight streamwise locations $x/H = 1, \dots, 8$, compared to the baseline results and the benchmark results obtained by direct numerical simulation [39].

It can be seen that the turbulent shear stress R_{12} in the baseline and benchmark results agree quite well with each other in the upper channel ($y/H = 2$ to 3) but deviate dramatically in the free-shear and recirculation regions. In the case with a small dispersion parameter $\delta = 0.2$, Fig. 7a shows that the uncertainty range as represented by the R_{12} samples is not able to cover the benchmark results in regions where large discrepancies exist between the baseline and benchmark. This indicates that the prior may be overly confident, which may



(a) Samples of k profiles, Case 1



(b) Samples of k profiles, Case 2

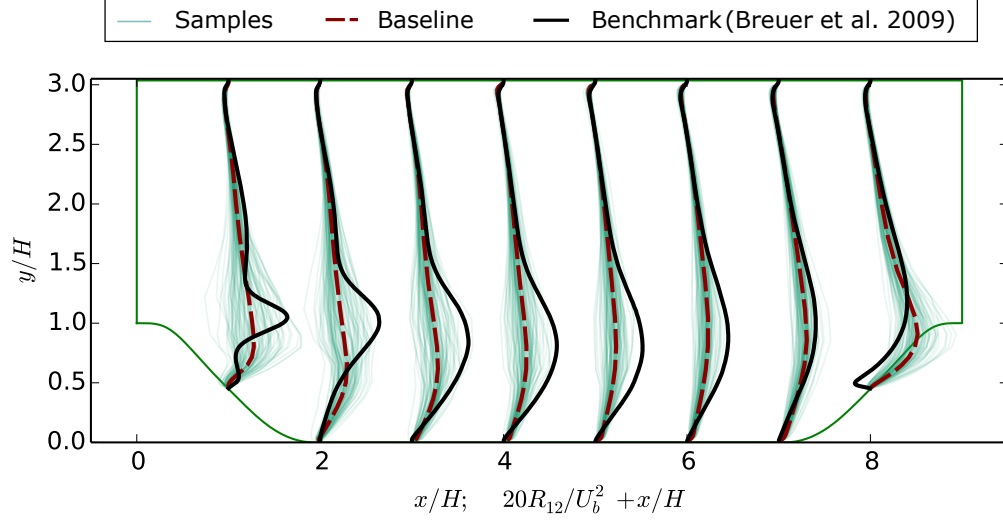
Figure 8: Comparison of sample profiles of turbulence kinetic energy k profiles for Case 1 and Case 2. The profiles are shown at eight streamwise locations $x/H = 1, \dots, 8$, compared to the baseline results and the benchmark results obtained by direct numerical simulation [39].

lead to difficulties in Bayesian inferences. With a large dispersion parameter $\delta = 0.6$ in Case 2, the scattering range of R_{12} increases and covers the benchmark in the entire domain, which is shown in Fig. 7b. However, since the dispersion parameter is spatially uniform, it also has large scattering in the upper channel, where in fact the discrepancies between baseline and benchmark results are rather small. Similar patterns are also observed in the turbulent kinetic energy k profiles, which are shown in Figs. 8a and 8b for Cases 1 and 2, respectively. However, a notable difference is that the range of samples is not able to cover the benchmark results even in Case 2 with a large discrepancy parameter. This is because the turbulent kinetic energy k is significantly underestimated in the baseline turbulence model, which is a known deficiency of turbulence models applied this flow. The deficiency stems from the fact that the shear stresses and consequently the modeled turbulent kinetic energy production are weaker than the physical counterparts [40].

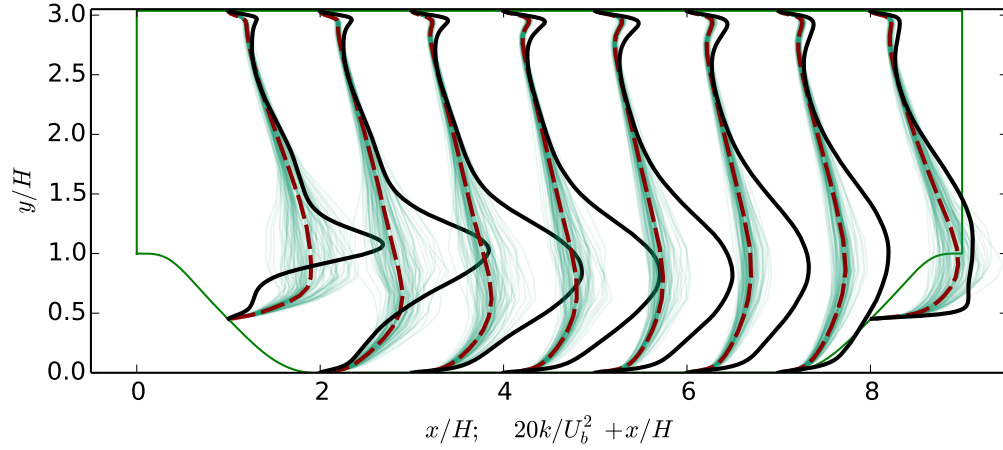
In light of the comparison between the samples and the benchmark above, it can be seen that using a spatial uniform dispersion parameter δ leads to scattering larger than necessary in the upper channel, but with insufficient scattering in regions that are indeed problematic for the baseline model (e.g., the free shear and recirculation regions). It is known from experiences in turbulence modeling that standard turbulence models have difficulties in these regions, using a nonuniform, informative dispersion field $\delta(x)$ as shown in Fig. 2 is justified in Section 4.1 above. The samples of R_{12} and k are presented in Fig. 9. In both cases the scattering of the samples are larger in the free-shear and recirculation regions and are smaller in the upper channel, which is more consistent with the actual discrepancies between the baseline and the benchmark results. A minor exception is that the turbulent kinetic energy near the upper wall is underpredicted by the baseline model but this is not reflected in the sample scatter, since this feature is not reflected in the prior knowledge in the dispersion parameter $\delta(x)$ field.

Overall speaking, all sample profiles of the Reynolds stress component R_{12} and the turbulent kinetic energy k shown in Figs. 7–9 are physically reasonable. These samples are qualitatively similar to those obtained with the physics-based approach by directly perturbing the physical variables C_1, C_2 , and $\ln k$ around the baseline results [7].

Ultimately it is the velocity fields and the associated auxiliary quantities (e.g., wall shear stress, reattachment point, and pressure drop across the channel) that are of interest in turbulent flow simulations. Therefore, the sampled Reynolds stress are propagated to velocities by using the RANS solver tauFoam [7], and the reattachment points are obtained by post-processing the velocity fields. The velocity profiles obtained for the three cases with



(a) Sample of R_{12} profiles, Case 3



(b) Sample of k profiles, Case 3

Figure 9: The sample profiles of turbulent shear stress R_{12} and turbulent kinetic energy k for Case 3. The ensemble profiles are shown at eight streamwise locations $x/H = 1, \dots, 8$, compared to the baseline results and the benchmark results obtained by direct numerical simulation [39].

different dispersion parameters are presented and compared in Fig. 10. Similar to the profiles of R_{12} and k , the velocity sample also show a small scattering in Case 1 ($\delta = 0.2$) and a larger scattering in Case 2 ($\delta = 0.6$). The advantage of using an informative $\delta(x)$ field can also be observed in this figure. Compared to the uniformly small scattering in Case 1 (panel a) and uniformly large scattering in Case 2 (panel c), the velocity scattering in Case 3 (panel c) is small in the upper channel and large in the free shear and recirculation regions, adequate to cover the benchmark results in both regions. Finally, we note that in all three cases the velocity scattering in the lower part, particularly in the recirculation region, of the channel is larger, even though the Reynolds stress scattering is spatially uniform in Cases 1 and 2. This observation suggests that the velocity in the recirculation region is more sensitive to the Reynolds stresses, an important physical insight that is provided by the RANS solver. Similar analyses have been performed on other quantities of interest including the bottom wall shear stress and the reattachment point. Qualitatively similar observations are made as those presented above for the velocities, and thus the figures for the other QoIs are omitted here.

5. Discussions

Whether the obtained maximum entropy distribution of Reynolds stress $[\mathbf{R}]$ should have zero measure on the two-component (and one-component) limiting states is an issue open for discussion. We explain below the implications based on the choices made in the proposed framework. Although practically we did not encounter this difficulty in this study, the discussion below adds to the theoretical completeness. The probability distribution for the normalized random matrix $[\mathbf{G}]$ as given in Eq. (10) has zero measure on the subset $\mathbb{M}_d^{+0} \setminus \mathbb{M}_d^+$ of singular positive semidefinite matrices, since $\det([G]) = 0$ in this set and thus $p_{[\mathbf{G}]}([G])|_{[G] \in \mathbb{M}_d^{+0} \setminus \mathbb{M}_d^+} = 0$. This is analogous to the χ^2 -distribution in the scalar case with more than three degrees of freedom. However, a valid distribution for semi-definite matrices could have a concentration of measure in the set of singular matrices, i.e., it is possible that $p_{[\mathbf{R}]}([R])|_{[R] \in \mathbb{M}_d^{+0} \setminus \mathbb{M}_d^+} \neq 0$. One can draw an analogy to the exponential distribution, for instance, in the scalar case. If the specified mean $[\underline{R}]$ of $[\mathbf{R}]$ is singular, i.e., $\det([\underline{R}]) = 0$, then $\det([\underline{L}_R]) = 0$. Consequently, any realization $[R]$ constructed from Eq. (8), $[\mathbf{R}] = [\underline{L}_R]^T [\mathbf{G}] [\underline{L}_R]$, is also singular since the distributive nature of determinants leads to $\det([R]) = 0$. The set $\mathbb{M}_d^{+0} \setminus \mathbb{M}_d^+$ of singular Reynolds stresses maps to the two-component limit edge ($C_3 = 0$) of the Barycentric triangle. This mapping can be explained by the fact that all matrices in this set have at least one eigenvalue that is zero (as they have zero

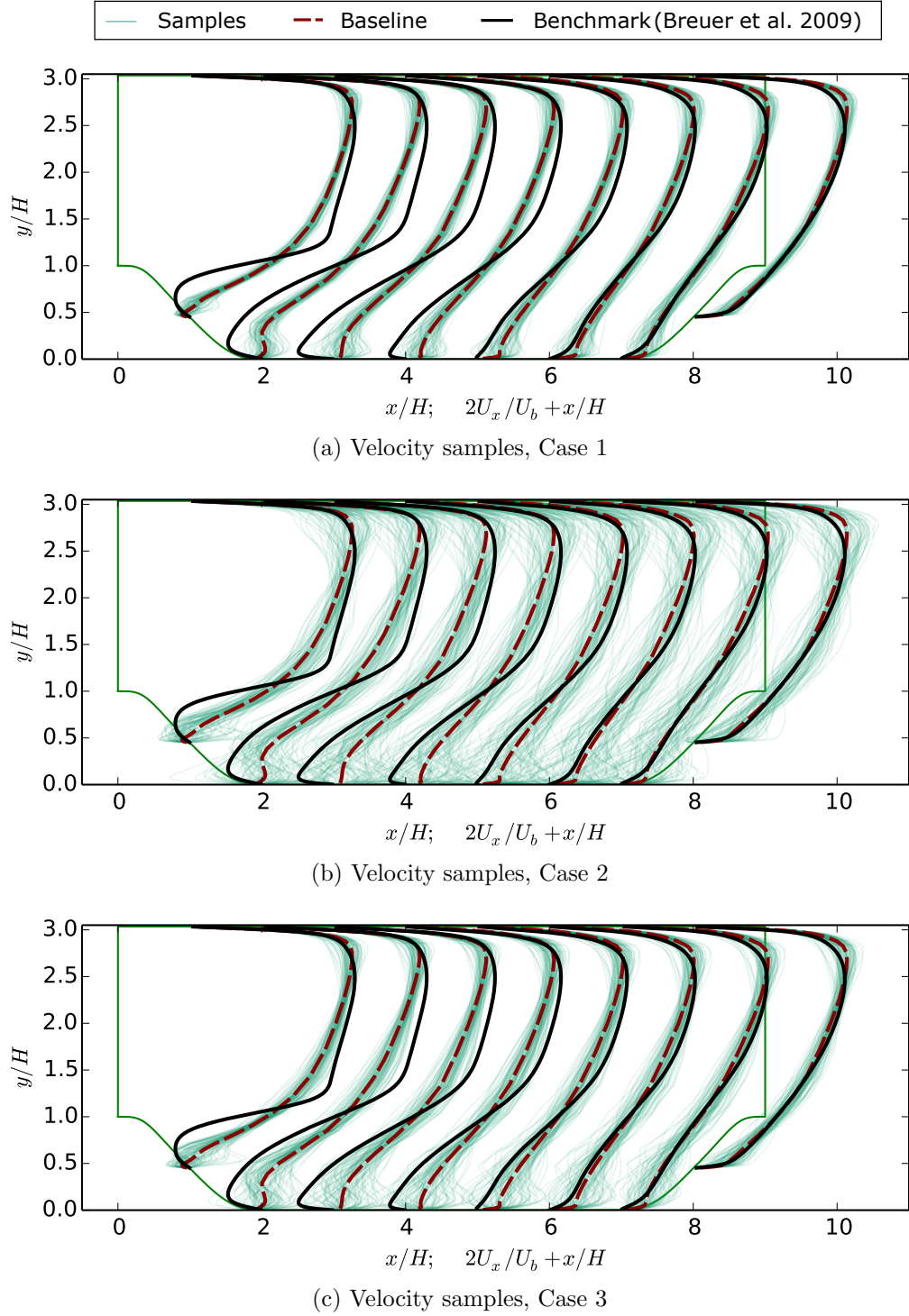


Figure 10: Comparison of propagated velocity profile samples for Cases 1, 2, and 3. The profiles are shown at eight streamwise locations $x/H = 1, \dots, 8$, compared to the baseline results and the benchmark results obtained by direct numerical simulation [39].

determinants), which corresponds to two-component turbulence. This correspondence is indicated in Fig. 1a. The physical interpretation of the mathematical consequences above can be summarized as follows:

1. When the specified Reynolds stress mean $[\underline{R}]$ corresponds to a turbulence state in a two-component limit, the samples of perturbed Reynolds stresses also have two-component states;
2. When the specified mean corresponds to a generic three-component state, the samples can become infinitely close to a two-component limit but has zero probability of falling on the limit.

6. Conclusion

In this work we propose a random matrix approach to guarantee Reynolds stress realizability for quantifying model-form uncertainty in RANS simulation. In this approach, the Reynolds stress field is described with a probabilistic model of a random field of positive semidefinite matrices with specified mean and correlation structure. The marginal probability distribution of the Reynolds stress at any particular location satisfies the maximum entropy principle. To sample such a random matrix field, Gaussian random fields with specified covariance kernel are first generated and then are mapped to the field of positive semidefinite matrices based on polynomial chaos expansion and reconstruction. Numerical simulations have been performed with the proposed approach by sampling the Reynolds stress and propagating through the RANS solver to obtain velocities. The simulation results showed that generated Reynolds stress fields not only have the specified statistics, but also are physically reasonable. The mathematically rigorous approach based on random matrix and maximum entropy principle is a promising alternative to the previously proposed physics-based approach for quantifying model-form uncertainty in RANS simulations. Moreover, it can be used to gauge the entropy of the prior distributions specified in the physics-based approach and thus to measure the information introduced therein. Detailed comparison between the two approaches will be pursued as follow-on work in the future.

References

- [1] S. B. Pope, Turbulent flows, Cambridge university press, 2000.

- [2] T. Oliver, R. Moser, Uncertainty quantification for RANS turbulence model predictions, in: APS Division of Fluid Dynamics Meeting Abstracts, Vol. 1, 2009.
- [3] L. Margheri, M. Meldi, M. Salvetti, P. Sagaut, Epistemic uncertainties in RANS model free coefficients, *Computers & Fluids* 102 (2014) 315–335.
- [4] M. Emory, R. Pecnik, G. Iaccarino, Modeling structural uncertainties in Reynolds-averaged computations of shock/boundary layer interactions, *AIAA paper 479* (2011) 1–16.
- [5] M. Emory, J. Larsson, G. Iaccarino, Modeling of structural uncertainties in Reynolds-averaged Navier-Stokes closures, *Physics of Fluids* 25 (11) (2013) 110822.
- [6] C. Górlé, G. Iaccarino, A framework for epistemic uncertainty quantification of turbulent scalar flux models for Reynolds-averaged Navier-Stokes simulations, *Physics of Fluids* 25 (5) (2013) 055105.
- [7] H. Xiao, J.-L. Wu, J.-X. Wang, R. Sun, C. J. Roy, Quantifying and reducing model-form uncertainties in Reynolds-Averaged Navier-Stokes simulations: An open-box, physics-based, bayesian approach, submitted. Available at <http://arxiv.org/abs/1508.06315> (2015).
- [8] J. L. Lumley, G. R. Newman, The return to isotropy of homogeneous turbulence, *Journal of Fluid Mechanics* 82 (01) (1977) 161–178.
- [9] S. Banerjee, R. Krahl, F. Durst, C. Zenger, Presentation of anisotropy properties of turbulence, invariants versus eigenvalue approaches, *Journal of Turbulence* 8 (32) (2007) 1–27.
- [10] J.-X. Wang, J.-L. Wu, H. Xiao, Incorporating prior knowledge for quantifying and reducing model-form uncertainty in RANS simulations, submitted. Available at <http://arxiv.org/abs/1512.01750> (2015).
- [11] J.-L. Wu, J.-X. Wang, H. Xiao, A Bayesian calibration-prediction method for reducing model-form uncertainties with application in RANS simulations, submitted. Available at <http://arxiv.org/abs/1510.06040> (2015).
- [12] C. E. Shannon, A mathematical theory of communication, *Bell System Technical Journal* 27 (1948) 379–423, 623–659.

- [13] E. T. Jaynes, Information theory and statistical mechanics, *Physical Review* 106 (1957) 620–630.
- [14] R. R. Coifman, M. V. Wickerhauser, Entropy-based algorithms for best basis selection, *Information Theory, IEEE Transactions on* 38 (2) (1992) 713–718.
- [15] S. C. Zhu, Y. Wu, D. Mumford, Filters, random fields and maximum entropy (FRAME): Towards a unified theory for texture modeling, *International Journal of Computer Vision* 27 (2) (1998) 107–126.
- [16] C. Soize, A nonparametric model of random uncertainties for reduced matrix models in structural dynamics, *Probabilistic engineering mechanics* 15 (3) (2000) 277–294.
- [17] S. Das, R. Ghanem, A bounded random matrix approach for stochastic upscaling, *Multiscale Modeling & Simulation* 8 (1) (2009) 296–325.
- [18] J. Guillemot, C. Soize, R. G. Ghanem, Stochastic representation for anisotropic permeability tensor random fields, *International Journal for Numerical and Analytical Methods in Geomechanics* 36 (13) (2012) 1592–1608.
- [19] M. Mignolet, C. Soize, Nonparametric stochastic modeling of linear systems with prescribed variance of several natural frequencies, *Probabilistic Engineering Mechanics* 23 (2) (2008) 267–278.
- [20] C. Soize, Random matrix theory for modeling uncertainties in computational mechanics, *Computer Methods in Applied Mechanics and Engineering* 194 (12) (2005) 1333–1366.
- [21] C. Soize, Stochastic modeling of uncertainties in computational structural dynamics – recent theoretical advances, *Journal of Sound and Vibration* 332 (10) (2013) 2379–2395.
- [22] S. B. Pope, *Turbulent Flows*, Cambridge University Press, Cambridge, 2000.
- [23] U. Schumann, Realizability of Reynolds-stress turbulence models, *Physics of Fluids (1958-1988)* 20 (5) (1977) 721–725.
- [24] J. L. Lumley, Computational modeling of turbulent flows, *Advances in applied mechanics* 18 (123) (1978) 213.
- [25] S. Pope, PDF methods for turbulent reactive flows, *Progress in Energy and Combustion Science* 11 (2) (1985) 119–192.

- [26] C. G. Speziale, R. Abid, P. A. Durbin, On the realizability of Reynolds stress turbulence closures, *Journal of Scientific Computing* 9 (4) (1994) 369–403.
- [27] B. E. Launder, D. Spalding, The numerical computation of turbulent flows, *Computer methods in applied mechanics and engineering* 3 (2) (1974) 269–289.
- [28] F. R. Menter, Two-equation eddy-viscosity turbulence models for engineering applications, *AIAA journal* 32 (8) (1994) 1598–1605.
- [29] P. R. Spalart, S. R. Allmaras, A one-equation turbulence model for aerodynamic flows, *Recherche Aerospatiale* 1 (1994) 5–21.
- [30] C. Gorlé, J. Larsson, M. Emory, G. Iaccarino, The deviation from parallel shear flow as an indicator of linear eddy-viscosity model inaccuracy, *Physics of Fluids* 26 (5) (2014) 051702.
- [31] H. Goldstein, *Classical Mechanics*, 2nd Edition, Addison-Wesley, 1980, see “The Euler Angles and Euler Angles in Alternate Conventions” in Chapter 4.4.
- [32] D. Stefanica, *A Linear Algebra Primer for Financial Engineering*, FE Press, 2014.
- [33] N. J. Higham, Analysis of the Cholesky decomposition of a semi-definite matrix, in: M. G. Cox, S. J. Hammarling (Eds.), *Reliable Numerical Computation*, Oxford University Press, 1990, pp. 161–185.
- [34] C. Soize, A comprehensive overview of a non-parametric probabilistic approach of model uncertainties for predictive models in structural dynamics, *Journal of sound and vibration* 288 (3) (2005) 623–652.
- [35] S. Sakamoto, R. Ghanem, Polynomial chaos decomposition for the simulation of non-Gaussian nonstationary stochastic processes, *Journal of engineering mechanics* 128 (2) (2002) 190–201.
- [36] O. P. Le Maître, O. M. Knio, *Spectral methods for uncertainty quantification: with applications to computational fluid dynamics*, Springer, 2010.
- [37] E. Dow, Q. Wang, Optimal design and tolerancing of compressor blades subject to manufacturing variability, in: *16th AIAA Non-Deterministic Approaches Conference*, American Institute of Aeronautics and Astronautics, 2014.

- [38] D. Xiu, Numerical methods for stochastic computations: a spectral method approach, Princeton University Press, 2010.
- [39] M. Breuer, N. Peller, C. Rapp, M. Manhart, Flow over periodic hills—numerical and experimental study in a wide range of reynolds numbers, *Computers & Fluids* 38 (2) (2009) 433–457.
- [40] F. Billard, Development of a robust elliptic-blending turbulence model for near-wall, separated and buoyant flows, Ph.D. thesis, The University of Manchester, Manchester, UK (2012).
- [41] J. C. Helton, F. J. Davis, Latin hypercube sampling and the propagation of uncertainty in analyses of complex systems, *Reliability Engineering & System Safety* 81 (1) (2003) 23–69.

Appendix A. Summary of the Algorithm of the Proposed Method

Given the mean Reynolds stress field $[\underline{R}](x)$ along with the correlation function structure of the random matrix field $[\mathbf{L}](x)$ as specified in Eq. (18), the following procedure is performed:

1. Expansion of given marginal distributions and covariances kernels:
 - 1.1. Perform the Cholesky factorization of the mean Reynolds stresses $[\underline{R}]$ at each cell according to Eq. (9), which yields field $\underline{L}_R(x)$ of upper triangular matrices.
 - 1.2. Perform KL expansion for the kernel function by solving the Fredholm equation (23) to obtain eigenmodes $\sqrt{\lambda_\alpha} \phi_\alpha(x)$.
 - 1.3. For off-diagonal terms only, perform polynomial expansion of the marginal PDF as described in Eq. (17) at each cell. Coefficients U_β are obtained from Eq. (27), where $\beta = 1, \dots, N_p$, and N_p is the number of polynomials retained in the expansion.
2. Sampling and reconstruction of random matrix fields for Reynolds stresses:
 - 2.1. For each element \mathbf{L}_{ij} of the random matrix field $[\mathbf{L}]$, independently draw N_{KL} sample from the standard Gaussian distribution $\omega_{ij,\alpha}$ where $\alpha = 1, \dots, N_{\text{KL}}$, e.g., with random sampling or Latin hypercube sampling method [41].

2.2. Synthesize realizations of the off-diagonal terms based on KL expansion:

$$\mathbf{w}_{ij}(x) = \sum_{\alpha=1}^{N_{\text{KL}}} \sqrt{\lambda_{\alpha}} \phi_{\alpha}(x) \boldsymbol{\omega}_{\alpha} \quad \text{with } i < j$$

$$\mathbf{L}_{ij}(x) = \sigma_d \mathbf{w}_{ij}(x)$$

2.3. Synthesize the realizations of the diagonal terms based on KL and PCE expansions:

$$\mathbf{u}_i(x) = \sum_{\beta=0}^{N_p} U_{\beta}(x) \Psi_{\beta}(\mathbf{w}_{ii}(x))$$

where the Gaussian random field sample $\mathbf{w}_{ii}(x)$ obtained in the previous step is used.

2.4. Synthesize the diagonal terms of matrix $[\mathbf{L}]$ from $\mathbf{L}_{ii}(x) = \sigma_d \sqrt{\mathbf{u}_i}$, where $i = 1, 2, 3$.

2.5. Reconstruct $[\mathbf{G}]$ from $[\mathbf{G}] = [\mathbf{L}]^T [\mathbf{L}]$ and then reconstruct the random matrix $[\mathbf{R}]$ from $[\mathbf{R}] = [\underline{L}_R]^T [\mathbf{G}] [\underline{L}_R]$.

3. Propagation the Reynolds stress field through the RANS solver to obtain velocities and other QoIs:

3.1 Use the obtained sampled Reynolds stress to velocity and other QoIs by solving the RANS equation.

3.2 Post-process the obtained velocity and QoI samples to obtain statistical moments.

Appendix B. Nomenclature

Subscripts/Superscripts

i, j	tensor indices ($i, j = 1, 2, 3$). Repeated indices do not imply summation.
α, β	indices for terms in Karhunen–Loeve and polynomial chaos expansions

Sets, operators, and decorative symbols

$\text{Cov}(\cdot, \cdot)$	covariance of two random variables
$\det(\cdot)$	determinant of a matrix
$\mathbb{E}\{\cdot\}$	expectation of a random variable
\mathcal{GP}	Gaussian spatial random process (random field)
\mathbb{M}_d^s	the set of all $d \times d$ symmetric matrices

\mathbb{M}_d^+	the set of all $d \times d$ symmetric, positive definite matrices
\mathbb{M}_d^{+0}	the set of all $d \times d$ symmetric, positive semi-definite matrices
$\text{tr}(\cdot)$	trace of a matrix
$\text{Var}(\cdot, \cdot)$	variance of a random variable
\ln	the natural logarithm
$\mathbb{1}_{\square}(\cdot)$	indicator function; takes value one if $\cdot \in \square$
$\vec{\cdot}$	vector
$[\cdot]$	matrix
$\underline{\square}$	mean value of variable \square
$\langle \cdot \rangle$	ensemble average/expectation of a random variable
$\ \cdot\ _F$	Frobenius norm
\sum	summation
\prod	product

Roman letters

$[A]$	anisotropy tensor of the Reynolds stress
$C_{[G]}$	normalization constant in the PDF of random matrix $[G]$
C_1, C_2, C_3	Barycentric coordinates
d	dimension of matrices ($d = 3$ implied unless noted otherwise)
$\vec{e}_1, \vec{e}_2, \vec{e}_3$	eigenvectors of tensor $[A]$
$[E]$	matrix formed by the eigenvectors of $[A]$, i.e., $[E] = [\vec{e}_1, \vec{e}_2, \vec{e}_3]$
$[\mathbf{G}], [G]$	a positive definite matrix with identity matrix $[I]$ as its mean
$[I]$	identity matrix
II, III	second and third invariants of tensor (3×3 matrix) $[A]$
K	kernel of a Gaussian process
$[\mathbf{L}], [L]$	an upper triangle matrix (e.g., obtained with Cholesky factorization)
l	length scale of Gaussian process
\mathbf{N}	Gaussian normal distribution
N_p	order of polynomial in the polynomial chaos expansion
N_{KL}	number of modes in KL expansion
p	probability density function
$[R]$	(negative of) Reynolds stress tensor with $R_{ij} = \langle u'_i u'_j \rangle$
$S(\cdot)$	entropy measure of a PDF
\mathbf{u}	random variable used to define the diagonal terms of matrix $[\mathbf{L}]$

\mathbf{v}_i	velocity at a particular location (random variable)
\underline{v}_i	mean velocity
\mathbf{v}'_i	the i^{th} component of the fluctuation velocity (random variable)
\mathbf{w}	standard Gaussian random variable, i.e., $\mathbf{w} \sim \mathbf{N}(0, 1)$
z, t	auxiliary variables

Greek letters

δ	dispersion parameter (uncertainty of the random matrix)
ν	variable indicating the order of the matrix
Γ	Gamma function
$\tilde{\lambda}_i$	eigenvalues of the turbulence anisotropy tensor $[A]$
Λ	3×3 diagonal matrix with eigenvalues of $[A]$ as elements, i.e., $\Lambda = [\tilde{\lambda}_1, \tilde{\lambda}_2, \tilde{\lambda}_3]$
$\lambda_\alpha, \phi_\alpha$	eigenvalues and basis functions of α^{th} mode obtained from KL expansion
Ψ_β	β^{th} order Hermite polynomial of the standard Gaussian random variable \mathbf{w}
Ω	spatial domain of the fluid flow field